https://doi.org/10.5194/egusphere-2025-6430
Preprint. Discussion started: 29 January 2026

Water Vapor Detection in Volcanic Plumes: Near-Infrared Cameras applications at Lascar, Chile, and Litli Hrútur, Iceland

Felipe Rojas Vilches[1], Tobias P. Fischer[1,2], Scott Nowicki[1], Melissa Anne Pfeffer[3], Felipe Aguilera[4,5], Tom D. Pering[6], Thomas Wilkes[6], Susana Layana[4,5], Cristóbal González[5], Matthew Fricke[7], John Ericksen[7], Melanie Moses[7]

[1] Department of Earth and Planetary Sciences, University of New Mexico, Albuquerque, NM, USA
[2] Department of Earth Science, University of California, Santa Barbara, CA 93106-9630 USA
[3] Icelandic Meteorological Office, Reykjavík, Iceland
[4] Universidad Andrés Bello, Facultad de Ingeniería, Antonio Varas 880, Santiago, Chile
[5] Millennium Institute on Volcanic Hazard Risk Research - Ckelar Volcanes, Avenida Angamos 0610, Antofagasta, Chile
[6] School of Geography and Planning, University of Sheffield, Sheffield, United Kingdom
[7] Computer Science department, University of New Mexico, Albuquerque, NM, USA

Correspondence to: Felipe Rojas Vilches (frojasvilches07@unm.edu)

Abstract. Water vapor (H_2O) dominates volcanic gas emissions globally with > 70 mol% of total volatile discharge, yet accurate H_2O flux measurements remain challenging due to high atmospheric background and H_2O's spectroscopic and physical complexities. We developed a multi-band near-infrared (NIR) camera system, calibrated with an in-situ Multi-GAS instrument to quantify volcanic H_2O flux. By combining plume speed measurement with H_2O absorption data, we derived the H_2O fluxes under favorable atmospheric conditions. We tested our approach at two contrasting volcanic settings: the passively degassing, high altitude, arid atmosphere Lascar volcano (Chile), and at the actively erupting, sea-level, humid atmosphere Fagradalsfjall volcano (Iceland) during the Litli Hrútur 2023 eruption. In November 26-29, 2022, and December 29, 2024, Lascar emitted 23,115 ± 10,694 t d^{-1} and 46,891 ± 18,863 t d^{-1} of H_2O, respectively, higher than previous estimates using traditional SO_2-based methods. In July/August 2023, the Litli Hrútur eruption averaged 19,108 ± 7,560 t d^{-1} of H_2O emissions, matching petrological estimates and steadily declining towards the end of the eruption. The simultaneous deployment of NIR camera, miniDOAS, and a UV camera prove that H_2O and SO_2 emissions vary independently, with Multi-GAS H_2O/SO_2 ratios fluctuating over time. This variability challenges traditional measurements and demonstrates that independent direct measurements of major gases (H_2O, CO_2, and SO_2) are essential for accurate volatile budgets and understanding volcanic degassing processes. Our work shows that the NIR camera approach provides a high-rate near-real time and direct method to obtain and visualize H_2O emission rates.

https://doi.org/10.5194/egusphere-2025-6430
Preprint. Discussion started: 29 January 2026

1 Introduction

High temperature magmatic and low-temperature hydrothermal volcanic vents emit gas constituents such as water vapor (H_2O), CO_2, SO_2, H_2S, HCl, HF, and CO, as well as trace components i.e., HBr, SF_6, H_2, and noble gases (Giggenbach, 1996; Oppenheimer et al., 2013). These volcanic emissions occur at passively degassing and actively erupting volcanoes and their compositions depend strongly on depth of the degassing magma chamber, the activity of the volcano and interaction of magmatic gases with a shallow hydrothermal system (Giggenbach, 1996). Typically, the three major magmatic gas constituents are H_2O, CO_2, and SO_2, which can make up over 98% of volcanic gases. In many cases, discharges from volcanic and hydrothermal vents contain between 70-98% of H_2O (Fischer and Chiodini, 2015). The collection and identification of these gases is critical for understanding degassing patterns, magma dynamics, hazards of eruptions (Sigurdsson and Carey 1986), impacts of gases on key sectors including aviation, agriculture, industry (Prata 2009, Luchi and Mutter 2020), and their atmospheric implications for climate change (Robock 2000, Schmidt et al., 2012; Jongebloed et al., 2023).

Despite being the dominant volcanic gas species, H_2O vapor is still a challenging species to detect and quantify, due to condensation and interactions with other particles in the plume. Additionally, H_2O content in volcanic plumes varies and depends on temperature, water vapor pressure, humidity, and aerosols particle sizes (Matsushima and Shinohara 2006; Herzog et al., 1998; Castillo et al., 2015). Fourier Transform Infra-Red and Open Path FTIR are commonly used methods in volcanology (Burton et al., 2000; Oppenheimer et al., 2006). However, these approaches have a complex retrieval process, which varies depending on available infrared light source used (Natural or artificial (Oppenheimer et al., 1998; Arellano et al., 2006; Platt et al., 2018). On the other hand, light-scattering remote sensing retrieval challenges are due to high atmospheric background levels and phase changes (vapor-droplet) occurring in the atmosphere (Girona et al., 2015, Kern et al., 2017; Kern 2025). Only a few studies on light-scattered remote-sensing quantification of volcanic H_2O emissions have been published to date, with the most successful quantification in dry, high-altitude environments.

Girona et al., (2013) made the first attempt to quantify volcanic H_2O emissions directly and remotely from Erebus volcano, Antarctica, using a traditional 3 channel Red-Green-Blue (RGB) camera. Pering et al., (2017) used an infrared camera arrangement to quantify H_2O in plumes from La Fossa Crater and Mt. Etna in Italy. Kern (2017) argued that using the technique of Pering et al., (2017) poses significant challenges to obtain H_2O readings, due to the difficulty to determine changes in relative humidity, unless optimal conditions are present, such as those in high altitude dry environments. Kern et al., (2017) used a portable Differential Optical Spectrometer (miniDOAS; Galle et al., 2002) optimized for visible wavelengths to detect H_2O in the plume of Sabancaya volcano, Peru, demonstrating the potential of the DOAS technique, and possibly other spectroscopic instruments, to accurately determine H_2O under favorable conditions.

Addressing concerns raised by Kern (2017), this paper revisits and refines the approach of Pering et al., (2017) using dual band near infrared image spectroscopy to quantify volcanic H_2O emissions. Our method takes into consideration the water droplets and is paired with independent in-plume gas measurements using a Multi-GAS system (Aiuppa et al., 2005; Shinohara, 2005) to measure the plume relative humidity, temperature, pressure, and gas composition (H_2O, CO_2, SO_2). These measurements

https://doi.org/10.5194/egusphere-2025-6430
Preprint. Discussion started: 29 January 2026

constrain the thermodynamic conditions of the plume, providing the necessary parameters to evaluate the near infrared absorption signal.

We base our work on the physical difference between the atmospheric background temperature and that of the plume, in which the warmer air of the plume allows to maintain a higher saturation vapor pressure over a span of time before the gas disperses its heat to the atmosphere (Lopez et al., 2015; Roberts et al., 2019; Cerminara et al., 2015). This approach considers that during this time the plume temperature is maintained at several degrees higher than the surrounding colder background air, allowing for excess in water vapor molecules to produce an increase in the 940 nm near infrared band, which is detectable as long as the condensation is not enough to obscure that absorption.

We quantified H_2O emissions from Lascar volcano, Chile, during passive degassing (non-eruptive) in November 2022 and December 2024, and from Fagradalsfjall during the July to August 2023 lava fountaining eruption at Litli Hrútur, in Iceland. The objective of this work is to show the capability to detect and quantify H_2O in volcanic plumes using near infrared remote sensing at very different environments from passive degassing and from erupting volcanoes. Most importantly, our integrated observational and modeling approach supports reliable H_2O detection in both dry, high-altitude environments and humid, low-altitude eruptive settings, highlighting the potential of H_2O remote sensing using near infrared absorption . We use our results to advance our understanding of water behavior in these two magmatic systems.

1.1 Lascar and Litli Hrútur Volcanoes

The passive degassing Lascar volcano in Chile and the July 2023 Litli Hrútur eruption in Iceland enabled us to study two end-member volcanoes in terms of H_2O emissions and atmospheric conditions. The contrasting environments of these volcanoes allowed us to assess the Near-Infrared camera performance under radically different conditions. Lascar volcano (23.37°S, 67.73°W, 5,490 m asl) located in northern Chile, is one of the most prominent volcanoes in the Central Volcanic Zone of the Andes (CVZA, Aguilera et al.,2022; Fig. 1). It is an andesitic stratovolcano composed of 2 edifices with 5 craters, the central being the most active (Matthews et al., 1997; Gardeweg et al., 1998; Tassi et al., 2009). The crater of Lascar is at high elevation in one of the driest deserts in the world. Extensive work has been done regarding satellite- and ground-based remote sensing, and characterization of gas compositions (Tassi et al., 2009; Tamburello et al., 2014; Lopez et al., 2015; Layana et al., 2020). Recently, Lascar volcano had a period of enhanced activity during January 2022, December 2022 (Global Volcanism Program, 2022), and January 2023 (Global Volcanism Program, 2023) with the most recent eruption occurring in January of 2023 (https://rnvv.sernageomin.cl/rnvv/TI_Santiago_prod/reportes_LB/2023/RAV_20230131_Antofagasta_v5.pdf) following a vulcanian eruption on December 2022.

https://doi.org/10.5194/egusphere-2025-6430
Preprint. Discussion started: 29 January 2026

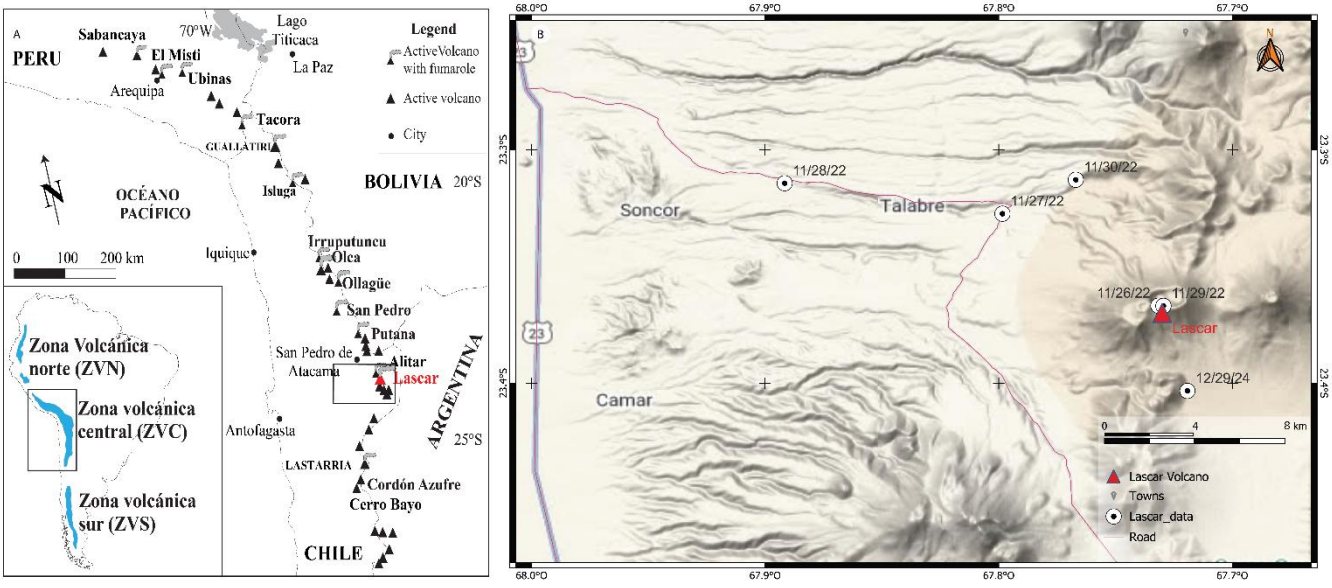

Figure 1 A) Location of the active volcanoes in the Central Volcanic Zone of the Andes (CVZA) shared between Peru, Chile, Bolivia, and Argentina. In red shows the location of Lascar volcano in the Antofagasta Region in Northern Chile. Taken and modified from de Silva and Francis, (1991) B) Topographic image of Lascar volcano with the most proximal highway to access the volcano and datetime locations of the measurements. All maps from: © Google (Earth) 2025, hybrid terrain.

Fagradalsfjall (63.92°N, 22.20°W) is one of the five volcanic complexes located in the Reykjanes Peninsula, an onshore continuation of the mid-Atlantic Reykjanes ridge, where the Reykjanes volcanic zone is the link to the mid-Atlantic Ridge (Thordarson and Larsen, 2007; Barsotti et al., 2023). This transtensional region (Fig. 2) has been volcanically active since 2021, with subsequent eruptions in 2022 and 2023 (Pedersen et al., 2025; Halldórsson et al., 2022; Parks et al., 2023; Caracciolo et al., 2023), ending a 781 year-long quiescent period without surficial activity (Sæmundsson et al., 2020). This volcanic region is at low elevation (300 m asl) and close to the ocean resulting in year-round high atmospheric humidity. The activity started on 10 July 2023 with a 1 km long fissure opening that, over the next few days, became focused in one vent on the SW of Kelir Mountain and at the foot of Litli Hrútur mountain. The eruption lasted for less than a month and was comparable to the 2022 eruption in size and intensity (Krmíček et al., 2023; Thordarsson et al., 2023).

https://doi.org/10.5194/egusphere-2025-6430
Preprint. Discussion started: 29 January 2026

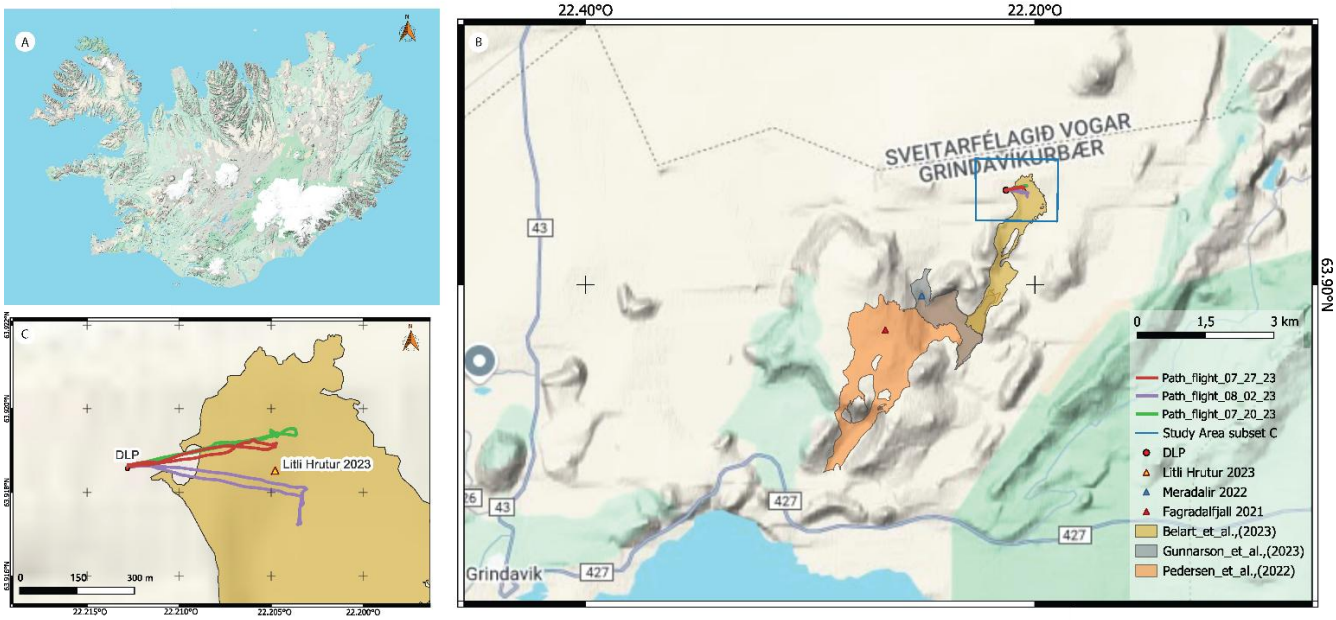

Figure 2 A) Simplified reference map for the study location in Iceland. B) The map illustrates the Fagradalsfjall lava flows extents, in red triangle the Geldingadalir 2021 (Pedersen et al., 2022), in blue triangle the Meradalir 2022 (Gunnarson et al., 2023), and yellow triangle for Litli Hrútur 2023. Additionally, the Drone Launch Point (DLP) is shown in red dot, same location for camera deployment. C) 3 drone flight examples from the launching point from the measuring site. All maps from: © Google (Earth) 2025, hybrid terrain.

2 Methods

2.1 Multi-GAS

The ground based Multi-GAS instrument (Shinohara, 2005; Aiuppa et al., 2005) measures CO_2 (SenseAir K33, SenseAir K30FR, and PP Systems SBA-5), CO (E4CO-100 Semea Tech, China), SO_2 (ES1-SO2-100 EC-Sense, Germany), H_2S (ES1-H2S-100 EC-Sense, Germany), and relative humidity (RH)-temperature (Sensirion SHT-3x; Fig. 3A). Additionally, we developed a UAV Multi-GAS version containing the K30FR CO_2, and the RH-Temperature sensor with either a CO or SO_2 sensor, which was mounted on a DJI Phantom 3 Pro (Fig. 3B), similar to the instrument used by Fischer et al., (2024). Among these, the SBA-5 analyzer has been successfully deployed in volcanoes (Stix et al., 2018; Ericksen et al., 2024), whereas the SenseAir NDIR sensors and electrochemical CO, H_2S, and SO_2 sensors are deployed here for the first time in volcanological applications.

At Lascar, we deployed the ground-based Multi-GAS with the K33 CO_2 sensor. At Litli Hrútur we deployed both the ground-based version with SBA-5 CO_2 and the UAV-Version with the K30FR. In all cases, our system sampled at a rate of ~0.3 standard liters per minute (slpm) with the inlet and outlet on opposite locations and recording the information on a single-board-computer (SBC) Beaglebone, which saved the information in separate CSV files, and the postprocessing was performed

https://doi.org/10.5194/egusphere-2025-6430
Preprint. Discussion started: 29 January 2026

using the software Ratiocalc 3.2 (Tamburello, 2015) to obtain the CO_2/SO_2, CO_2/H_2O, and H_2O/SO_2 ratios using data with at least a $R^2 > 0.6$ (Battaglia et al., 2019, Kazahaya et al., 2022). These ratios can then be used to derive H_2O and CO_2 fluxes from SO_2, and SO_2 and CO_2 from H_2O fluxes (Aiuppa et al., 2008; Conde et al., 2014; Fischer et al., 2019). We propagated the uncertainty of all methods when using this approach.

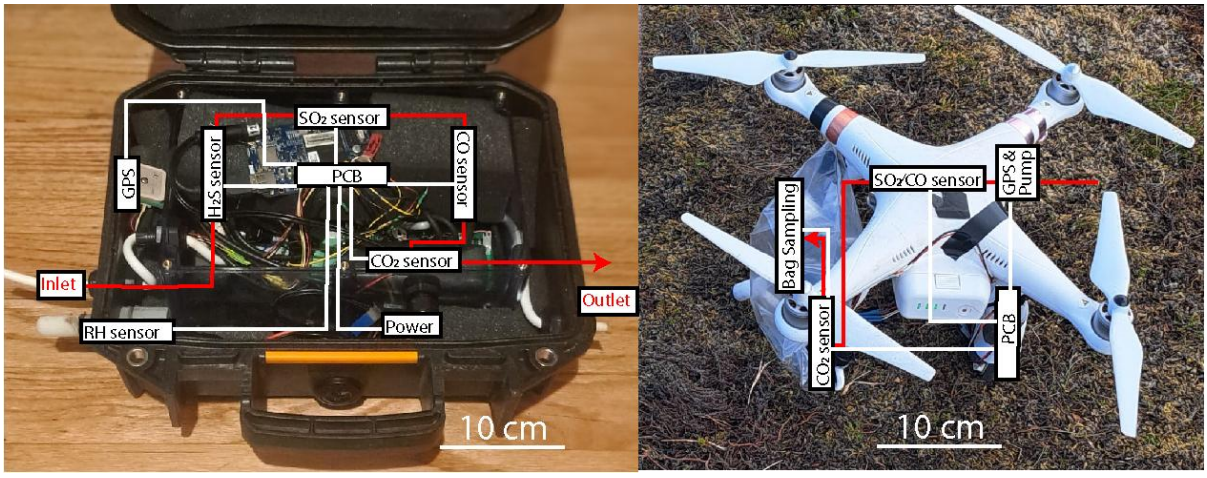

Figure 3 A) Multi-Gas system in the enclosed and portable Pelican case. B) Multi-GAS system in the field with a Tedlar bag attached for gas collection (Fischer et al., 2024). The White lines are physical connections to the main PCB board and red lines are the flow directions connected with tubing.

2.2 Near-Infrared (NIR) camera system

2.2.1 System hardware, image acquisition and preprocessing

We developed a multi-camera system (Fig. 4) that consists of five co-incident cameras, including two near infrared filtered webcams (Logitech C300), a visible light (VIS) Raspberry Pi camera (No IR camera v2), and two long-wave infrared cameras (Flir Boson, results not discussed in this work). These cameras were connected via USB to a minicomputer Raspberry Pi to record images and time stamps using a connected GPS module. Each NIR camera has a narrow bandpass absorption filter mounted in front of the original optics, although the internal near-infrared blocking filter was removed from the optical path. The two spectral filters are meant to measure the reflected and scattered sunlight on and off the NIR water vapor absorption feature (Fig. 5). The bandpass are centered at 940 nm at 850 nm respectively, with ~10 nm full width at half maximum (FWHM). The 940 nm absorption region has been shown to be a viable method to obtain H_2O data for radiometers (Halthore et al., 1997; Ingold et al., 2000; Momoi et al., 2020,; Pérez-Ramírez et al., 2012). This window of absorption is used to calculate the non-scattering H_2O vapor emitted by the volcano, aided by a calibration performed with our Multi-GAS instrument that directly measures gas concentrations within the plume (section 3.1), following the approach of Pering et al., (2017). In addition, we calculated CO_2 and SO_2 emissions from this system measured H_2O fluxes and the Multi-GAS ratios.

https://doi.org/10.5194/egusphere-2025-6430
Preprint. Discussion started: 29 January 2026

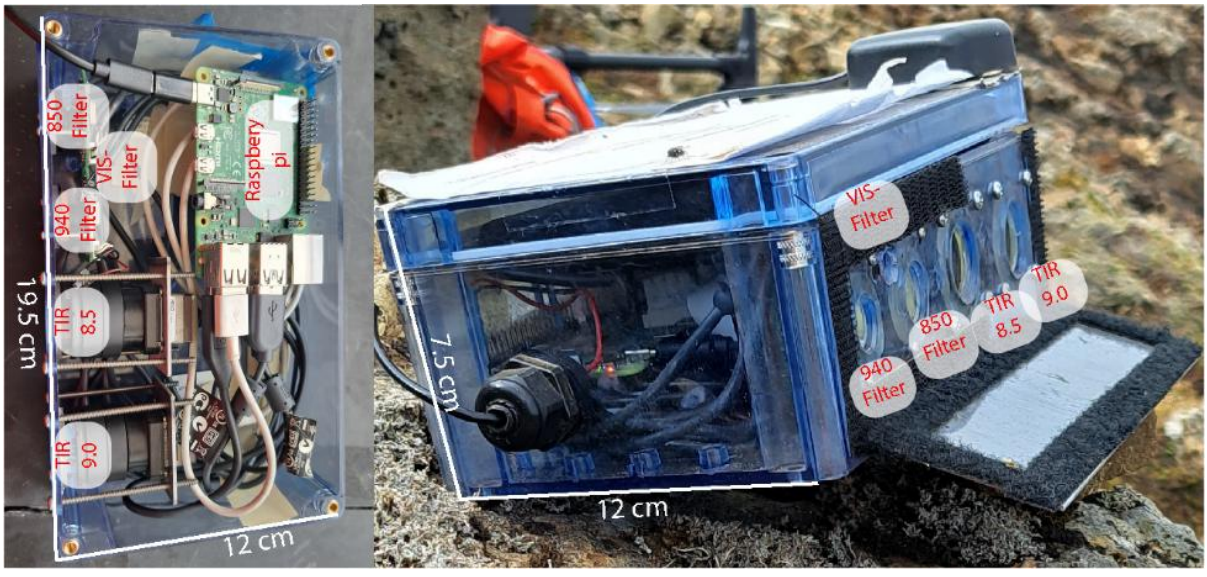

Figure 4 NIR camera with the labels for each filter and element.

The NIR cameras are Charged Coupled Devices (CCD) with a good response curve in regions ~1000 nm (Langer et al., 2013. The optics are focused on infinity to maximize perpendicular light entering the sensor. The field of view (FOV) of the cameras used here are not precisely optically aligned but rather are generally aligned on the system and the imagery geometry is adjusted during post-processing using a computer vision image transformation algorithm. The effect is that images are aligned at the pixel scale, although we typically downscale the resolution by a factor of 4. Images are recorded as 16-bit uncompressed (YUY2) format, providing a raw intensity image that the camera chip does not compress to byte. Images are acquired within less than 0.2 seconds of each other, with best-efforts to reduce the lag time between writing co-incident imagery to the storage drive. The camera controls, acquisition, and post-processing were performed by using a self-developed Python code. For the acquisition, a Graphic User Interface (GUI) was used to allow maximum control over settings, which includes exposure, brightness, saturation, white balance, and gain. From this GUI, the essential parameters are the exposure rate and gain. These parameters need adjusting to obtain the maximum intensities for specific light conditions, avoid saturation of the images, and set the signal-to-noise ratio (SNR) for all subsequent images (Lübcke et al., 2014). The proper adjustment of exposure and gain was accomplished by adjusting the histogram of the images as close to a Gaussian curve and centering the absorption.

Figure 5 shows the absorption of H_2O and the locations of the bands used for this study with the camera response function at those wavelengths. Because the consumer-grade NIR cameras have a Bayer-filter pattern adhered to the pixels on the sensor array, there are three spectral responses that we can choose from to combine with the external narrow-band filters. We only use the red pixels in our calculations because the red channel is broadly sensitive to the entire spectral region from 550 to >1000 nm, while blue and green have functions that do not provide a continuous spectral response (Cheremkhin et al., 2014). This gives the best light throughput when the camera response function (green line) is multiplied by the narrow-band filter functions (orange and blue lines), as is the case with multiple filters in the optical path.

https://doi.org/10.5194/egusphere-2025-6430
Preprint. Discussion started: 29 January 2026

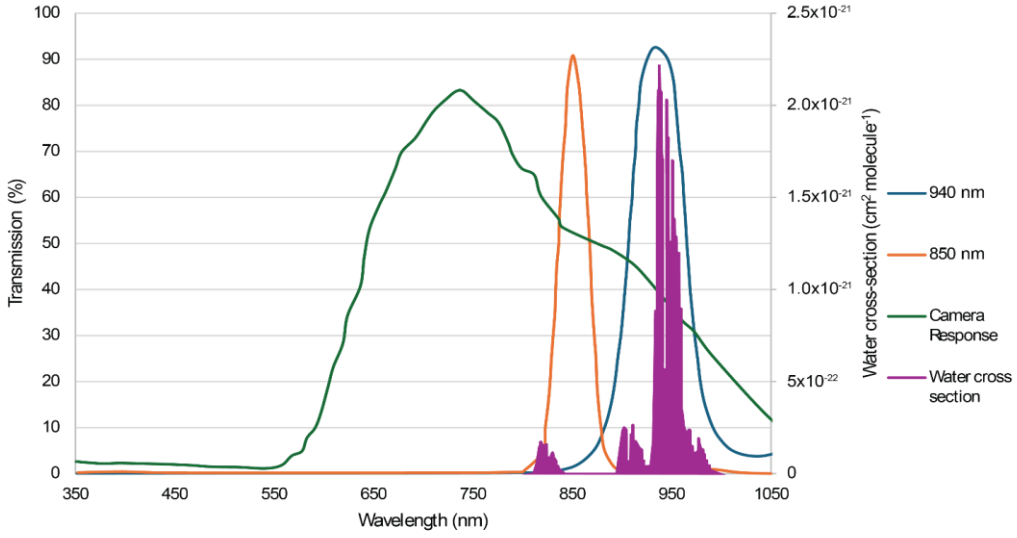

Figure 5 Percent transmittance of the two band-pass filters used (850 nm and 940 nm) for construction of the H_2O camera. In green is shown the camera percent transmittance and in magenta the absorption cross-section for H_2O as individual lines. It is important to note that this system does not distinguish individual lines but is sensitive to the integral over several bands.

2.2.2 Water vapor, calculation and calibration

Volcanic plumes, like the atmosphere, contain water as a mixture of different phases. The gas phase of water in volcanic plumes is controlled by the vent exit temperature and the ability of the plume to maintain a higher temperature than the surrounding atmosphere as it moves away from the vent. This effect can change the appearance of the plume, roughly represented by its color and transparency. Condensed water droplets in the plume will give its opaque-white plume color (Matsushima and Shinohara, 2006; Kern et al., 2017). We can show the plume H_2O vapor concentration dependence on the temperature and pressure at which it is obtained by using the Wagner and Pruβ (2002) formulation for H_2O saturation vapor pressure as follows:

$$ln\left(\frac{pws}{Pc}\right) = \frac{Tc}{T}(C_1 v + C_2 v^{1.5} + C_3 v^3 + C_4 v^{3.5} + C_5 v^4 + C_6 v^{7.5}) \quad (1)$$

$$v = 1 - \frac{T}{Tc} \quad (2)$$

Where Pws is the saturation water vapor, Pc is the critical pressure (constant), v referred to as the Transformed temperature, Tc is the critical temperature (constant), T is temperature, C_x are constant coefficients. The relative humidity can be calculated as the percent ratio of H_2O pressure (Pw) to the saturation H_2O pressure (Pws), and by using the ideal gas law, we can obtain the H_2O content (equation 3).

$$\frac{kg}{m^3} = \frac{Mw_{H_2O} * P}{R * T} \quad (3)$$

https://doi.org/10.5194/egusphere-2025-6430
Preprint. Discussion started: 29 January 2026

Where Mw_{H_2O} is the molar weight of water, P is pressure, R is the ideal gas constant, and T is temperature. Figure 6 shows the strong dependence of H_2O saturation on air temperature. The values in Fig. 6 represent 100% relative humidity (saturation) at each temperature, showcasing how warmer air can hold significantly more H_2O. The same principle is maintained for volcanic plumes since the temperature difference between the plume and surrounding atmosphere will create a notable difference; (Cerminara et al., 2015), allowing the air parcel to sustain a higher concentration of H_2O molecules in the vapor phase. In other words, warmer plumes can carry more H_2O as vapor, which directly influences the observed H_2O emissions.

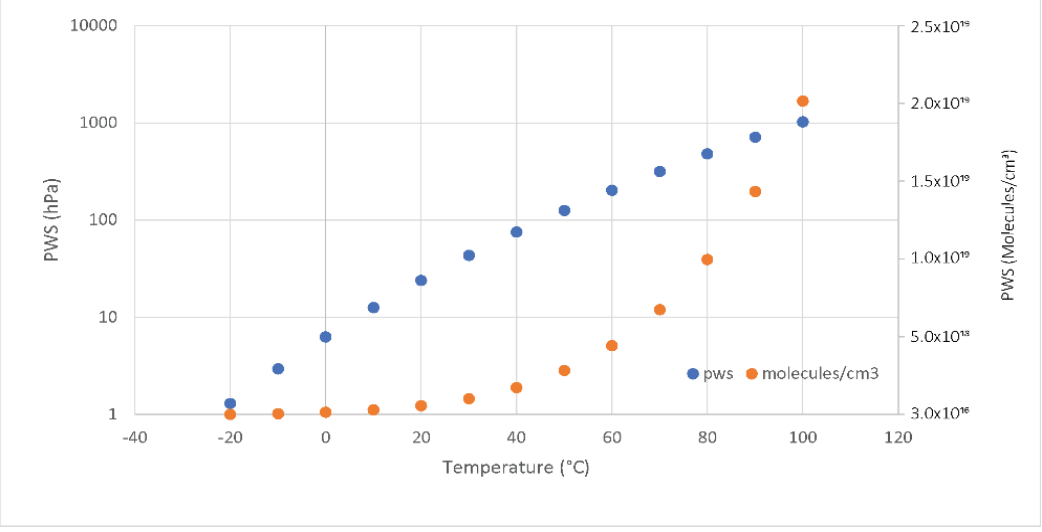

Figure 6 Calculated H_2O saturation pressure (Pws) using standard pressure with Wagner and Pruβ (2002). Important features of the graph are the sharp variation in H_2O molecules as temperature changes.

For most camera systems, calibration gas cells are used to determine the concentration of a scene by placing the known concentration cells in front of the lenses, allowing to create a response curve and effectively converting them to ppm*m (Mori and Burton 2006; Kuhn et al., 2023). For the case of H_2O, this methodology would be difficult to apply, and the scene is also a function of pressure, humidity, and temperature (Kern et al., 2017; Girona et al., 2015; Pering et al., 2017). Therefore, for our calibrations we selected the highest measured values of the plume from the Multi-GAS humidity sensor (SHT-3x) and discriminated using the SO_2 and CO_2 sensors to distinguish in-plume water vapor. This approach allows us to obtain H_2O concentrations in ppmv at a specific location within the plume. Then, we converted the pixels signal of the cameras to total measured water using Ratiocalc 3.2 (Tamburello 2015), which applies a variation of the McRae (1980), and the Wagner and Pruβ (2002) formulation for calculating the H_2O concentrations, using temperature (°C), relative humidity (%), and pressure (hPa). This is similar to the approach of Pering et al., (2017) for H_2O and Pering et al., (2014) for high-resolution CO_2 imaging, setting a precedent for this calibration method across multiple gases. We then used a site-specific factor to estimate the concentration in $kg*m^{-3}$ based on the molecular weight of water, the ideal gas law at the plume temperature and pressure conditions (equation 3). Finally, we calculated the flux by integrating the converted value considering the plume width, wind speed, and estimated thickness, obtained either by measuring the vent dimensions or through visual observation in the field,

https://doi.org/10.5194/egusphere-2025-6430
Preprint. Discussion started: 29 January 2026

and corroborated with other field measurements when possible (i.e. miniDOAS traverses). Figure 7 shows the Multi-GAS and the camera system approach for obtaining measurements in a volcanic gas plume.

The relationship and effect of temperature, pressure, and humidity on the retrieval of H_2O of volcanic plumes has not been carefully considered, although it has been considered and addressed for SO_2 (Horrocks et al., 2001). We assume H_2O behaves like an ideal gas and is the main constituent of the plume (>75-95%). Therefore, we do not apply partial pressure corrections (Dalton's law) because it would not be significantly impacted by other gases.

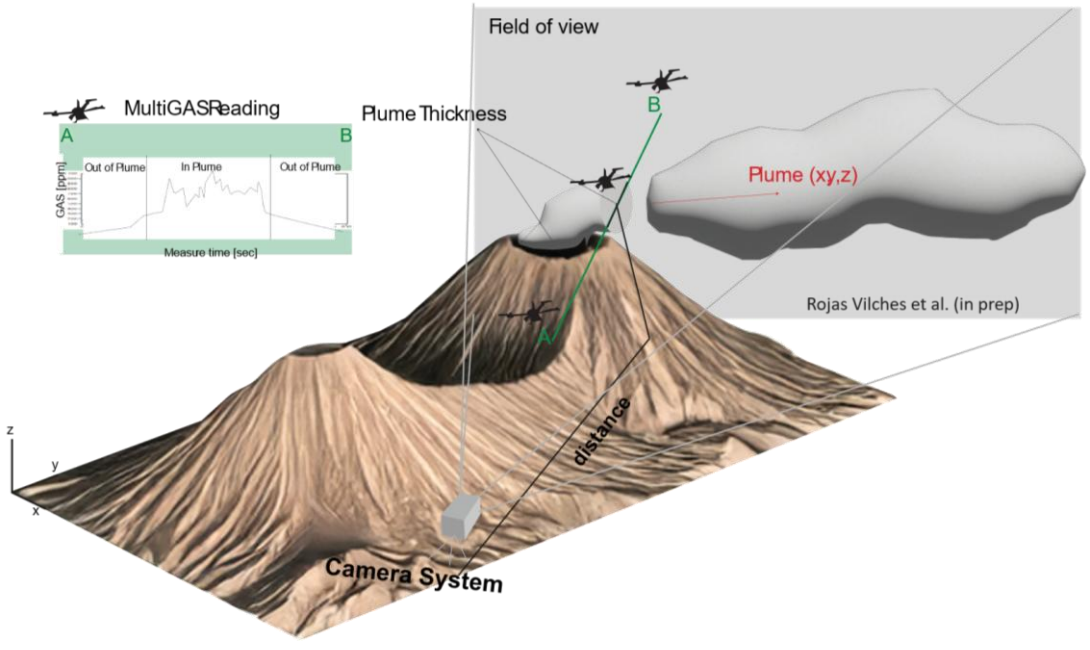

Figure 7 3D view of the camera and A-B transect made with a Multi-GAS going through the volcanic plume. In the drawing, the camera is at (x, y) distance from the source of the volcanic plume. This volcanic plume has an initial thickness similar to the volcanic

2.2.3 Water vapor absorption, flux estimation, and validation

Although H_2O is abundant in the atmosphere, this approach focuses on the retrieval of the excess H_2O concentration in volcanic plumes relative to the background air, due to elevated temperatures, which increases the saturation vapor pressure (Wagner and Pruβ, 2002), allowing plumes to transport significantly more H_2O particles in an air parcel compared to the background. This difference is quantifiable by using the Beer-Lambert law, similar to the approach using SO_2 cameras (Kern et al., 2010; Lübcke et al., 2014; Kern 2025). The Beer-Lambert law (equation 4) states that the light attenuation due to a gas can be described by the radiance spectrum I(λ), which is related to the gas absorption coefficient k in the specific wavelength λ along a light path x as follows:

$$\frac{dI(\lambda,x)}{dx} = -k_a(\lambda,x)I(\lambda,x) \quad (4)$$

This method for determining H_2O vapor is a similar approach as for the SO_2 cameras acquisition methods (Mori and Burton 2006; Bluth et al., 2006), and we follow similar steps to those that are used for data acquired by SO_2 cameras (Kantzas et al.,

https://doi.org/10.5194/egusphere-2025-6430
Preprint. Discussion started: 29 January 2026

2010), including the dark offset correction, flatfield (overall brightness) corrections, and selecting a background region. The images should show a higher concentration of H_2O increasing towards the horizon (bottom of the image) where most of the water vapor column resides due to longer light path through the lower atmosphere. Therefore, the selected background region has to be as close to the horizon as possible if clear-sky conditions allow it, because the background region could introduce systematic errors.

In addition, as the presence of water droplets in the atmospheric column produces a visible scattering of light, the VIS imagery is used to correct for the presence of water droplets by normalizing both channels for these scattering effects, and to exclude imagery when the scattering effect becomes too significant to correct. This method applies a standard brightness correction to both co-incident NIR images by subtracting a single-band VIS brightness image from each. As this approach is performed using three initially uncalibrated camera arrays. This is a relative adjustment that relies on an in-situ measurement to calculate the absolute value of any of the derived data products. However, as we are using raw, uncompressed 16-bit value for all the images, this method should not be highly affected by overall brightness in the scene caused by sun angle, if all the images are collected at the same time. Although this approach uses different spectral regions than those utilized for other gases, our approach is similar to previously published multi-band methods for gas retrievals (Nowicki, 2020; Xiong et al., 2022).

We then divided each plume image (IPx) by its corresponding background region (IBx) and proceeded to apply the Beer-Lambert law for the filters 940 nm (H_2O absorbent) and 850 nm (non-absorbent), respectively, to obtain the apparent absorbance (AA) as follows: (equation 5)

$$AA = -\ log\left(\frac{\frac{IP_{940-dark}}{IB_{940-dark}}}{\frac{IP_{850-dark}}{IB_{850-dark}}}\right) \quad (5)$$

The measured differential absorption between the plume and background is then converted to absolute concentration using in-situ Multi-GAS measurements of the plume temperature, relative humidity, and pressure (Section 2.2.1) and the plume thickness. These were used to calculate Integrated Column Amounts (ICA) over the plume width. ICAs represent the sum of H_2O column density per line of sight above the background threshold.

To estimate the ICA we require the pixel size of the image, which is calculated using simple trigonometry (equation 6)

$$Pixel_{size} = \frac{(tan\left(\frac{FOV}{2}\right) \times 2 \times distance)}{Image\ resolution} \quad (6)$$

The FOV (Field of View) is the maximum viewing angle previously measured, and the distance is measured using GIS-software between the camera (obtained by GPS) to the center of the plume/crater, and the image resolution. The plume speed (v) is then calculated using the cross-correlation method (McGonigle et al., 2005; Mori and Burton, 2006; McGonigle et al., 2009), which uses two parallel ICA transects drawn across the plume and perpendicular to the emission or wind direction. The time it takes for the signal of gas to travel across both segments of known distance gives plume speed. For this work, each measurement sequence was divided into shorter segments to calculate plume velocities independently. We report the minimum and maximum plume speeds obtained across all segments of the sequence and considered them limit values. We use half of this range to represent the average value of plume speed, which was used to estimate the fluxes of H_2O in tons per day (t d^{-1}).

https://doi.org/10.5194/egusphere-2025-6430
Preprint. Discussion started: 29 January 2026

While a comprehensive study and characterization of the detection limit is beyond the scope of this study, we performed HITRAN radiative transfer simulations (Rothman et al., 2012) using field atmospheric parameters for each site. For both simulations we use the HITRAN Hapi API (Rothman et al., 2012). The expected relative radiance and optical depth were calculated for an "expected plume" and using atmospheric specific values for temperature and pressure for both volcanoes, similar to those shown in (Kern 2017). The simulations, described in more detail in appendix A1 and A2, demonstrate that the differential absorption is valid and measurable for both locations, though more strongly under high altitude and low humidity conditions, although Litli Hrútur has an added caveat due to the infrared light being emitted from the lava at the eruption site which makes it is not only a full solar light scattering problem but complicates the calculations by adding infrared radiation emitted from the vent. Estimating the proportion of each, however, goes beyond the scopes of this article. With the above, the best working conditions for this method are >10 °C difference between plume and ambient, with a clear sky background, and at distances closer than 6 km. For validation, we used temperature and wind data collected by the Dirección Meteorológica de Chile (DMC) weather station located in llano Chajnantor (5,100m asl; accessed in December 2022 https://climatologia.meteochile.gob.cl/application/diariob/visorDeDatosEma/230021) and the Iceland Meteorological Office (IMO) at Lastar and Fagradalsfjall, for Chile and Iceland, respectively.

2.2.4 Error sources and uncertainty propagation

Flux scales linearly with plume speed, which is the main source of uncertainty in our calculations. For each sequence we calculated the plume speed error (σ_v) using the plume speed ranges (equation 7)

$$\sigma_v = \frac{(v_{maximum} - v_{minimum})}{(v_{maximum} + v_{minimum})} \quad (7)$$

where $v_{maximum}$ and $v_{minimum}$ are the maximum and minimum plume speeds from image analysis. This method results in low errors (~5%) for stable atmospheric and plume conditions, and high errors (~60%) for unstable conditions, with typical uncertainties within that range. These plume speed ranges, along with anemometer data allow us to assess real emission changes due to wind variability. We recorded wind speed with a handheld anemometer near the camera deployment whenever possible.

We only quantified wind speed uncertainty, but other sources of uncertainty in our system include the Multi-GAS sensor precision of ±0.1 °C for temperature and ±1% RH. Additionally, The assumption that the plume is homogeneous is not entirely correct and the measurement of plume gas composition is affected by this heterogeneity. Hence, the Multi-GAS total water measurement can have an additional 5-15% error due to spatial and temporal variations of the plume composition and dimensions. We assumed a calibration error of 5-10% for favorable Multi-GAS measurements near the emission point.

For SO_2 and CO_2 NIR-derived fluxes, we propagated the uncertainty by calculating the total relative error as the sum of their individual instrument/software measurement uncertainty.

https://doi.org/10.5194/egusphere-2025-6430
Preprint. Discussion started: 29 January 2026

2.3 DOAS

We used a miniature differential optical absorption spectroscopy instrument (miniDOAS; Galle et al., 2002) model USB2000+ spectrometer from Ocean Optics® commonly used in volcanic applications to obtain SO_2 fluxes (Kern et al., 2009, 2017; Arellano, 2013; de Moor et al., 2013). In addition, we used the miniDOAS data along with the Multi-GAS system to calculate the emitted CO_2 and H_2O flux measurements at each site, using the H_2O/SO_2 or CO_2/SO_2 Multi-GAS ratios (Aiuppa et al., 2008; Conde et al., 2014; Fischer et al., 2019).

At Lascar, we used DOAS SO_2 emission reports and data from the local volcano monitoring agency Observatorio Volcanologico De los Andes del Sur (OVDAS), a program of the Chilean National Geology and Mining Service (SERNAGEOMIN) to perform these calculations. At Litli Hrútur, we performed walking and car traverses for transects across the plume (Galle et al., 2002). The spectrometer was mounted vertically on a backpack and plume transects were perpendicular to the wind direction. We recorded clear sky background and blackbody reference spectra on either side of the plume. Wind speed and direction were measured in the field using a handheld anemometer and compass, we used IMO wind speed report using two wind directions and two measured speeds to estimate uncertainty of our field data. Data acquisition and processing were completed using the open-source MobileDOAS software (https://github.com/NOVACProject/MobileDOAS). The H_2O and CO_2 miniDOAS-derived values were obtained similarly to NIR-derived values.

2.4 UV Camera

At Litli Hrútur we obtained SO_2 emission data and at Lascar volcano we use data obtained by the Millennium Institute on Volcanic Risk Research - Ckelar Volcanes (from now on referred as Ckelar) using a UV Camera system provided by University of Sheffield (Mori and Burton 2006, Bluth et al., 2006; Wilkes et al., 2017; Wilkes et al., 2018). For each measurement, we followed the approach of Lübcke et al., (2014) collecting a dark image, a clear sky image for overall brightness correction, and performed a calibration by using gas cells of known SO_2 concentration (Kern et al., 2025). We performed calibrations each time we made a measurement to ensure similar light conditions (approximately every hour). We processed the images using the manufacturer's software and a Python code to obtain the plume speeds and SO_2 fluxes using a cross-correlation technique (Mori and Burton, 2006; Wilkes et al., 2016; Wilkes et al., 2023). In addition, we calculated the standard deviation of the obtained data and used it as a first order uncertainty of the technique. To calculate other gases fluxes we employed the same as the DOAS system using the SO_2 fluxes and the measured Multi-GAS ratios and propagated the uncertainties as explained for the NIR system.

3 Results

We include an introduction to the location, data collected, and the settings used in each method. For the UV camera and NIR cameras, we refer to the data as sequences, which are a series of images taken in a continuous timeframe. The results are

https://doi.org/10.5194/egusphere-2025-6430
Preprint. Discussion started: 29 January 2026

summarized in tables, organized by the method used (as presented in the method section), and location. The information is further detailed by volcano, with Multi-GAS data presented as molar ratios.

Supplementary Material Fig. S1 shows stack images for each day of measurements per volcano. Additionally, we provide supplementary videos with the sequences distinguished by the type of technique (NIR or UV) followed by date.

3.1 Lascar Volcano, Chile

We recorded plume gas data on November 26-29, 2022, and 29 December 2024 using the Multi-GAS system and obtained plume images using our NIR camera and the Ckelar permanent SO_2 camera (Wilkes et al., 2023). The locations (Fig. 1) were selected based on dominant wind direction and previous SO_2 camera site deployments (Lopez et al., 2015, Wilkes et al., 2023, Ckelar research group, pers.com.). The NIR cameras were set to capture at a rate of one image per 1-4 seconds and tested at varying distances from the crater to a maximum of 17.1 km, at altitudes between 3,240 to 5,478 m asl. However, the farthest distances were limited by image quality, signal dilution and atmospheric effects, and therefore were not included in the final analysis.

To obtain plume composition and calibration, we used the Multi-GAS system on the crater rim of Lascar to collect plume data on November 26 and 29, 2022, and December 29, 2024, at 5,478 m asl. We also performed Multi-GAS background atmospheric measurements near the town of Talabre, at the foot of the volcano and at an elevation of 3240 m asl. These measurements provided constraints for evaluating and validating the NIR signal.

3.1.1 Multi-GAS

Table 1 summarizes the gas data collected at Lascar volcano using both Ckelar and out Multi-GAS system. On October 13, 2022, the Ckelar instrument measured H_2O/CO_2 of 19.1 ± 6.7 inside the crater and 1150.7 ± 654.1 on the crater rim. On November 12, 2022, the same instrument calculated 253.8 ± 186.5 H_2O/SO_2. The instrument's CO_2 sensor malfunctioned after November 13. However, it was able to record data with the other sensors, including relative humidity and temperature, resulting in an estimate of a maximum of 19,816 ppmv H_2O. On November 26, 2022, the system measured 86.5 ± 26.8 H_2O/SO_2.

Our Multi-GAS system measured relative humidity data on November 26, 2022, and December 29, 2024, recording a maximum of 10,600 ppmv and 21,670 ppmv H_2O, respectively at the crater rim. For background reference, we used the temperature (23.3°C) and relative humidity (18%) measured in Talabre (3300m asl) as representative conditions for both the November 2022 and December 2024 campaigns.

3.1.2 NIR camera

Using the NIR camera system, we collected 6 sequences with a total of 13,945 images, 4,971 with the 850 nm filter, 4,000 images with the 940 nm filter, and 4,974 images using the VIS camera. The discrepancy in the total images collected by the 3 cameras is the result of a bug in the acquisition code that caused multiple images to be taken between single shots. The same

https://doi.org/10.5194/egusphere-2025-6430
Preprint. Discussion started: 29 January 2026

issue forced the camera to take images with only 1 filter on November 26, 2022, preventing further processing. Fig 8 shows the most representative processed images with their corresponding cross correlation columns and background per day.

Table 2 shows the parameters used with the NIR camera system, along with the measured H_2O fluxes and calculated CO_2 and SO_2 fluxes. All flux calculations are based on H_2O/SO_2 ratio of 86.5 ± 26.8 and a H_2O/CO_2 ratio of 19.1 ± 6.7 from Multi-GAS data obtained by Ckelar in October 2022 to November 2022 (Table 1).

On November 27, 2022, the camera was situated ~8 km from the crater and acquired images for 37 minutes, though only measurements for 9.5 minutes provided valid data. The wind speed calculation for this sequence is 7.9 to 20.2 m s^{-1} which yields a H_2O flux of 34,787 ± 15,283 t d^{-1} and yields a calculated flux of 1,430 ± 1,071 t d^{-1} SO_2 and 4,449 ± 3,515 t d^{-1} CO_2.

On November 28 the NIR camera was situated at Talabre town (~17 km west of the crater) and too far to collect valid data.

On November 30, 2022, with the camera system located 6.2 km to the west of the crater, we obtained 2 sequences of 11 and 21 min each. The first measured a H_2O flux of 12,143 ± 5,914 t d^{-1} with plume speeds of 4.76-13.8 m s^{-1} This resulted in a calculated a flux of 499 ± 398 t d^{-1} SO_2 and 1,553 ± 1,301 t d^{-1} CO_2. The second sequence measured an H_2O flux of 22,415 ± 10,884 t d^{-1} with plume speeds of 4.19-12.10 m s^{-1}. This yielded a calculated flux of 922 ± 773 t d^{-1} SO_2 and 2,867 ± 2,398 t d^{-1} CO_2.

On December 29, 2024, the NIR camera was located 4.3 km to the southeast of the crater, and we obtained 2 sequences. The first measured a H_2O flux of 46,891 ± 18,863 t d^{-1}, with a cross-correlation speed of 3.15 to 7.39 m s^{-1}, consistent with anemometer measurements of 5-10 m s^{-1} and gusts of 14 m s^{-1}. These measurements yield a calculated flux of 1,928 ± 1,373 t d^{-1} SO_2 and 5,997 ± 4,516 t d^{-1} CO_2. The second sequence measured a H_2O flux of 112,968 ± 79,479 t d^{-1}, with plume convection and stagnation at the center of the crater that prevented precise plume speed calculations using the cross-correlation method. The calculated plume speeds range from 3.00-17.24 m s^{-1}. Though still in the range of field measured wind speeds of 6-14 m s^{-1}, the data is unreliable. Using the H_2O fluxes resulted in calculated fluxes of 4,644 ± 4,707 t d^{-1} SO_2 and 14,449 ± 15,234 t d^{-1} CO_2.

3.1.1 miniDOAS

The monthly average SO_2 flux reports are publicly accessible (https://rnvv.sernageomin.cl/volcan-lascar) and are presented in Table 3, along with calculated H_2O and CO_2 emissions based on a H_2O/SO_2 ratio of 86.5 ± 26.8 from Multi-GAS data obtained by Ckelar in October 2022 to January 2023 (Table 1) and the average CO_2/SO_2 from in-situ fumaroles above 100°C from Tassi et al., (2009) of 19.0 ± 6.7.

In October 2022, SERNAGEOMIN reported a monthly average of 764±47 t d^{-1} SO_2 flux, with a maximum of 1,224 t d^{-1} SO_2, yielding a calculated H_2O flux of 18,583 ± 6,901 t d^{-1} and CO_2. flux of 9,972 ± 4,130 t d^{-1} For November, emissions decreased to an average of 424 ±46 t d^{-1} SO_2 flux and maximum of 1,031 t d^{-1} SO_2, yielding a calculated H_2O flux of 10,313 ± 4,314 t d^{-1} and a CO_2 flux of 5,534 ± 2,552 t d^{-1}. The emissions continued to decline in December, with reported averages of SO_2 flux of 285 ±46 t d^{-1} and a maximum of 869 t d^{-1} SO_2, resulting in a calculated H_2O flux of 6,932 ± 3,267 t d^{-1} and a CO_2 flux of 3,720 ± 1,912 t d^{-1}. Following the December 8, 2022, eruption, emissions increased in January 2023 to an average SO_2 flux of

https://doi.org/10.5194/egusphere-2025-6430
Preprint. Discussion started: 29 January 2026

483 ±74 t d^{-1} and a maximum SO_2 flux of 881 t d^{-1}2. Based on this, we calculate a flux of 11,748 ± 5,440 t d^{-1} H_2O and 6,304 ± 3,189 t d^{-1} CO_2 using the traditional method. On December 2024, SERNAGEOMIN reported average SO_2 flux of 293 ± 63 t d^{-1} and maximum of 717 t d^{-1} SO_2. Using Multi-GAS ratios, these fluxes yield 7,127 ± 3,740 t d^{-1} of H_2O and 3,824 ± 2,171 t d^{-1} of CO_2.

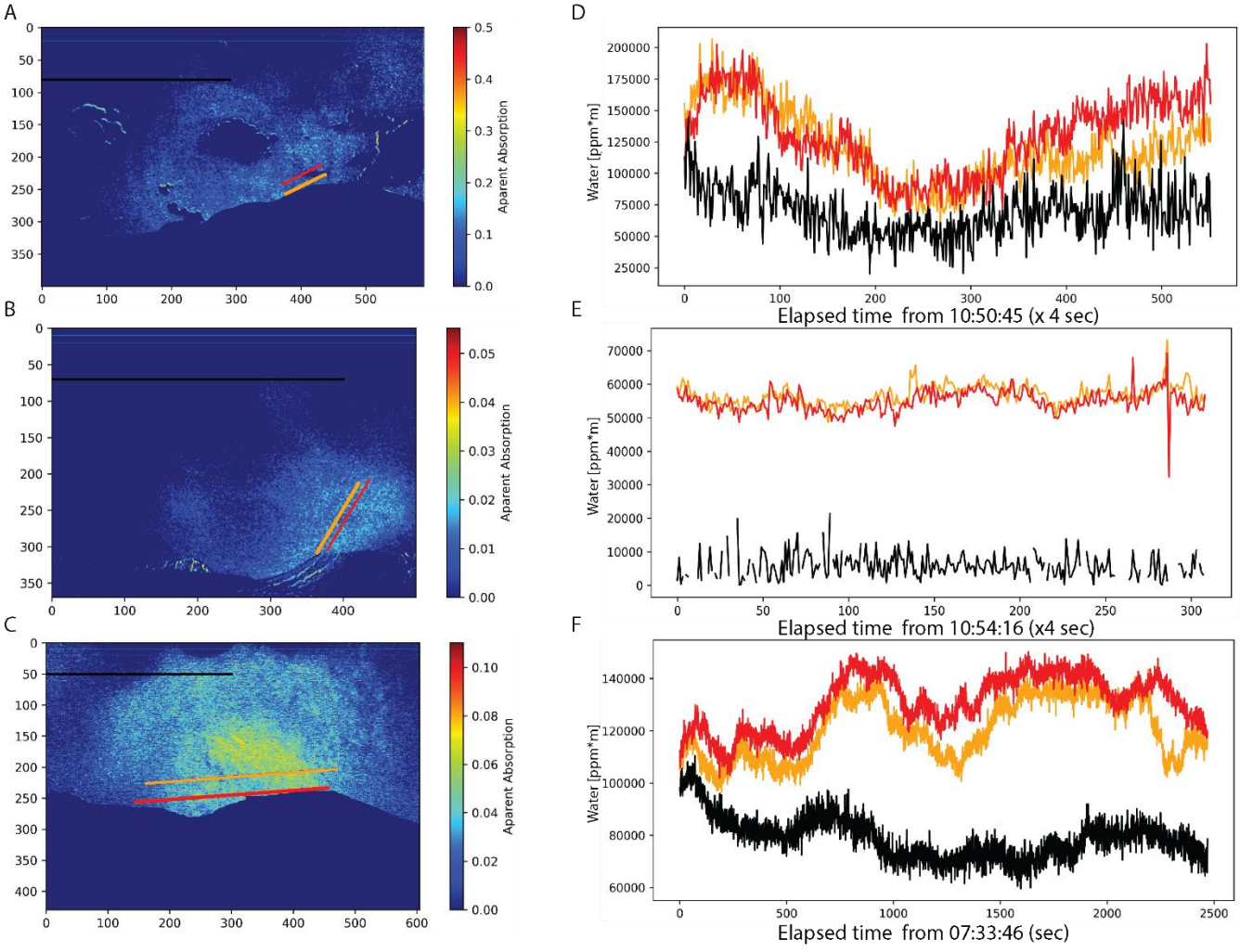

Figure 8 Representative image obtained at Lascar with the drawn Integrated column amounts for the sequences of A) November 27, B) November 30, and C) December 29, with their respective column amounts (D, E, and F). The warm colors show a higher H_2O content in the cool (dark blue) background. The orange and red lines were used for determining plume speeds.

3.1.2 UV Camera

UV camera data were collected by Ckelar during field campaigns in January and May 2022. Representative images from the sequences with a sample calibration curve are presented in Fig 9 A and B, with data shown in Table 4. The system was calibrated using gas cells of 100, 467, and 1989 ppm*m SO_2. H_2O and CO_2 fluxes were calculated using the same method that

https://doi.org/10.5194/egusphere-2025-6430
Preprint. Discussion started: 29 January 2026

we applied for the DOAS system, which combines the measured SO_2 flux data with the H_2O/SO_2 Multi-GAS ratios from Ckelar and CO_2/SO_2 of 19.0 ± 6.71 measured by Tassi et al., (2009) for fumaroles above 100°C.

On January 27, 2022, we measured an SO_2 flux of 338 ± 115 t d^{-1} using calculated plume speeds of 7.9 m s^{-1}On January 28, the SO_2 flux increased to 903 ± 100 t d^{-1} with a calculated plume speed of 8.1 m s^{-1} On May 31, the calculated SO_2 flux was 105 ± 4 t d^{-1} using a plume speed of 14.3 m s^{-1} Calculated H_2O and CO_2 fluxes are summarized in Table 4.

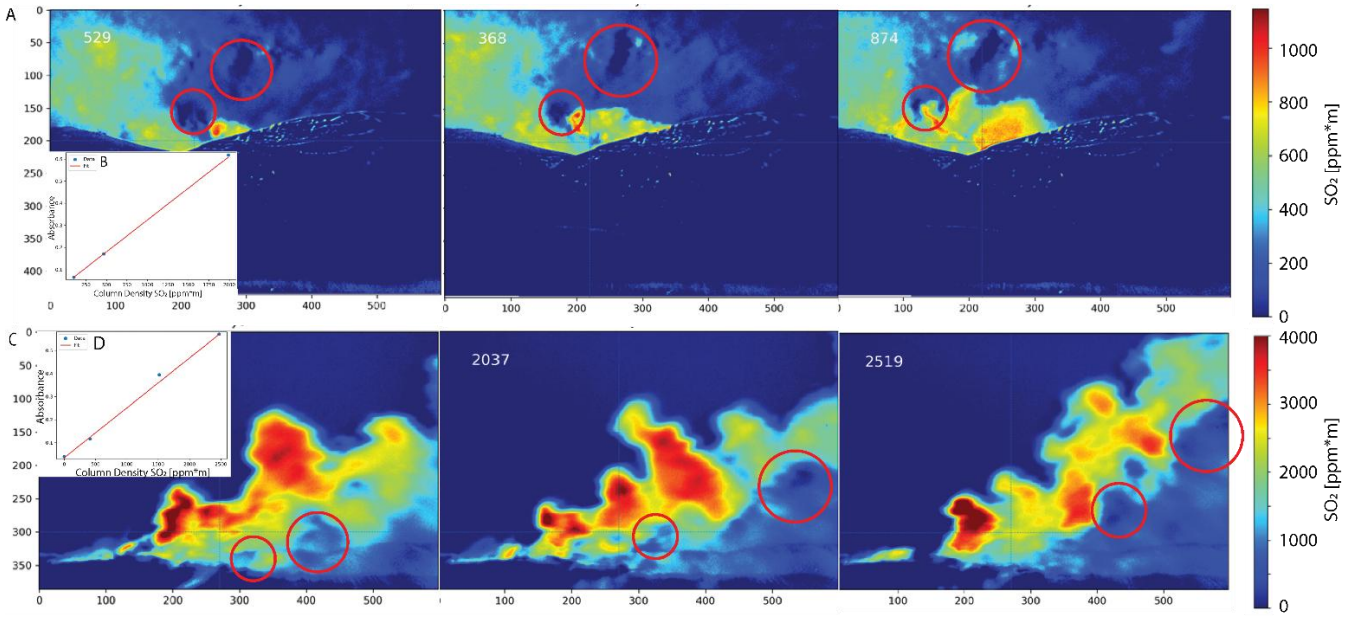

Figure 9 A Sequence of images obtained with the UV camera system by Ckelar research group on the day 27 January 2022. B Sequence of images obtained with the UV camera system on August 2,2023, during the Litli Hrútur 2023 eruption. Both sequences show their corresponding SO_2 absorbance curve calculated from the calibration images and using a linear fit (inlets B and D).

3.2 Litli Hrútur

We collected data from the Fagradalsfjall volcano, Iceland, during the Litli Hrútur eruption between July 19 to August 2, 2023. The UV camera and NIR camera were located at a perpendicular distance of ~450 m to the plume (Fig. 2) and at an elevation of 220 m asl. The NIR camera captured one set of images per 2-4 seconds for periods of 2-3 hours depending on plume and light conditions. The UV camera captured images at 4 seconds rate for about 20 min on July 28 and August 2, 2023.

We used our ground-based Multi-GAS system, placed ~400 m west of the active crater on July 19, 21, 22, and 25 of 2023. We successfully flew the UAV-based Multi-GAS system 30 to 80 m above the erupting lava pond on July 24, 27, and 28 of 2023 and August 2, 2023. Additionally, we collected miniDOAS data during the same days as we collected the Multi-GAS data.

Figure 10 contains a visual evolution of the Litli Hrútur eruption, detailing plume transparency and color, moss fires, and the overall cloud coverage, all of which gives a representative view of available sunlight (UV-NIR). We performed parallel measurements with Multi-GAS and the NIR camera system on July 24, 25, 27, 28 and August 2, 2023, adding the UV camera

https://doi.org/10.5194/egusphere-2025-6430
Preprint. Discussion started: 29 January 2026

on July 28 and August 2, 2023. Observations with miniDOAS were collected by car or walking traverses on the same days as our Multi-GAS collection, plus July 14,providing further context.

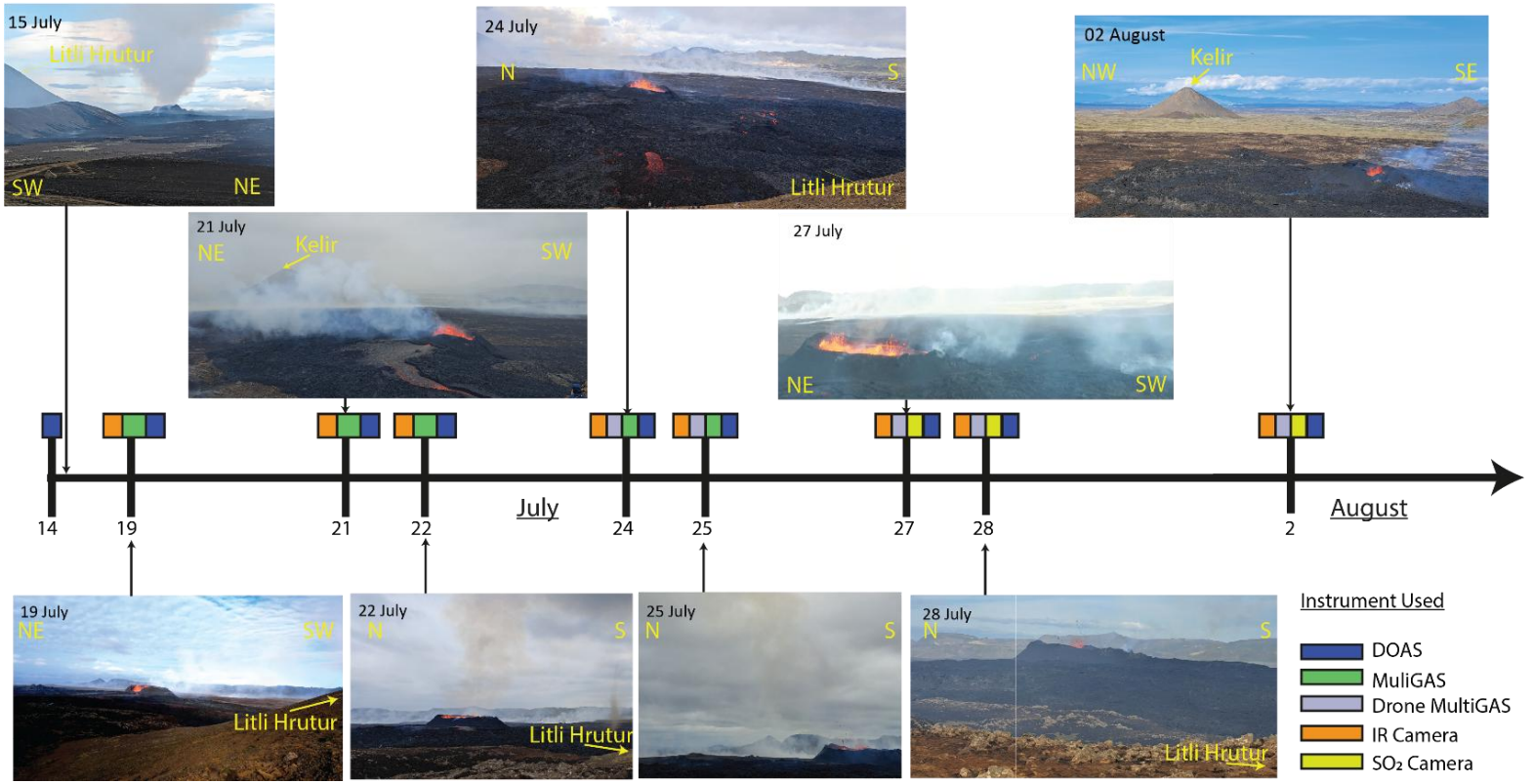

Figure 10 Timeline for Litli Hrútur eruption 2023. The eruption shows the instruments used each day to collect data over the months of July and August.

https://doi.org/10.5194/egusphere-2025-6430
Preprint. Discussion started: 29 January 2026

3.2.1 Multi-GAS

The ground-based Multi-GAS was 200 m from the UAV launch point (Fig. 2), which was ~400 m from the crater's active lava pond. Due to a malfunction of the SO_2 sensor we only calculated 41.3 ± 23.9 H_2O/CO_2, however this ratio is highly likely contaminated by moss fires and too far from the source, therefore will not be considered hereafter.

The UAV Multi-GAS measured CO_2 concentration, temperature, relative humidity and either SO_2 or CO concentrations. H_2O estimates were obtained using standard pressure with the RH and temperature of the sensors. The SO_2 concentration was also used to identify the volcanic H_2O emissions by using the peak of SO_2 in the measured timeframe. Table 1 shows molar ratios of H_2O/CO_2, H_2O/SO_2, and CO_2/SO_2 with R^2>60% confidence for 8 days of UAV and portable Multi-GAS measurements. The H_2O/CO_2 ratios helped differentiate plumes from moss fires and the H_2O/SO_2 ratios were obtained from this first discriminant. The drone-based Multi-GAS calculated between 5.9-199.6 H_2O/CO_2, 72.2-168.7 H_2O/SO_2, and 5.1-23.3 CO_2/SO_2 from July 21 to August 2, 2023 (Table 1). The gases released from the Litli Hrútur eruption over the period of 1 month, have average ratios (R^2>0.6) of CO_2/SO_2= 5.6 ± 2.8 , H_2O/SO_2= 126.0 ± 66.5, and H_2O/CO_2=11.1± 10.7 measured by Multi-GAS. The high uncertainty of the H_2O/CO_2 can be explained with the noise of the sensors, which can be seen in the inlet of Fig 11 for CO_2, this could be reduced but we kept data averaging filter consistent for all gases at 5 units. These averages do not include the H_2O/CO_2 ratios obtained on July 21, 28, and August 2 because of possible contamination by emissions from moss fires

3.2.2 NIR Camera

Between July 19, 2023, and August 2, 2023, we collected NIR camera data on 8 separate days, totaling 49,278 images, 16,680 with the 850 filter, 15,926 with the 940 filter, 16,672 using the VIS camera (~13 hrs. of data; Table 2). For H_2O vapor fluxes, we used Multi-GAS data and visual field observations to estimate the minimum thickness of the plume (~40 m) based on crater size. Figure 11 shows a full calibration procedure and Figure 12 show the cross correlation with a corresponding reference image. Additional supplementary videos for the valid sequences are also provided.

On July 19, 2023, we calculated a plume speed between 13.67-14.75 m s^{-1} and obtained H_2O fluxes between 20,291 ± 771 t d^{-1} using the measured H_2O concentration of 13,600 ppm. Using a H_2O/CO_2 of 17.0 and H_2O/SO_2 of 72.2 from our Multi-GAS data (Table 1), we calculated fluxes of 999 ± 898 t d^{-1} SO_2 and 2,916 ± 3,044 t d^{-1} CO_2. The cloud covered background and light conditions on July 21 and July 22 did not allow us to estimate the volcanic H_2O (Fig. 10 and Fig. 12 B). For July 21, we were able to calculate a plume speed of 27.1 m s^{-1}, which far exceeds anemometer wind speed field measurements of 7.0-9.1 m s^{-1}, the discrepancy might be because we obtained the gas plume speed for July 21 close to the vent, though it can also be explained due to noise being the same as our H_2O signal, and therefore the integration lines are not able to pick up a cross-correlation speed. The same difficulty was seen on July 22.

On July 24 we observed a semi cloudy background with windows of clear sky and moss fires that started expanding (Fig. 10) but did not affect our measurements (Fig. 12 D and K). Figure 12 D shows the 2 different sources of the signal, one at ground level and another at the crater, with different traveling altitudes. This allowed us to calculate plume speeds between 1.4 and

https://doi.org/10.5194/egusphere-2025-6430
Preprint. Discussion started: 29 January 2026

5.3 m s^{-1} using the NIR camera a comparable value to the anemometer wind speeds of 3.3-4.2 m s^{-1}, giving a H_2O flux of 20,094 ± 11,862 t d^{-1}. With these measurements we calculated SO_2 fluxes of 990 ± 1,436 t d^{-1} and CO_2 fluxes of 2,887 ± 4,609 t d^{-1}.

On July 25 the sky and light conditions worsened, with the recorded anemometer windspeed of 3 m s^{-1}, we estimated a H_2O flux of 2,064 t d^{-1} for a short window of minutes due to tourists blocking FOV of the volcano. Similar conditions persisted on July 27, where the background and lights conditions were non-ideal. Additionally, fires affected our FOV and only ~30 minutes of data were valid. Nevertheless, as is shown in Fig. 12 E and L, the system was barely able to resolve the plume close to the source resulting in 2,919 ± 645 t d^{-1} of H_2O flux, and a calculated SO_2 flux of 144 ± 155 t d^{-1} and CO_2 flux of ,1209 ± 1,402 t d^{-1} using Multi-GAS a H_2O/SO_2 ratio of 72.2 and a H_2O/CO_2 ratio of 5.9.

On July 28, 2023, the fires and clouds (Fig. 10) created a challenge to calculate plume speed. Using the measured H_2O concentration of 30,200 ppm with the Multi-GAS and relying on anemometer data of 4.2-5.6 m s^{-1} we estimated H_2O fluxes between 6,185 ± 884 t d^{-1}, with background variability being different to the measured ICA (Fig. 12 M). This yielded an SO_2 flux of 144 ± 85 t d^{-1} and a CO_2 flux of 1,400 ± 560 t d^{-1}, using the Multi-GAS averages of 10.8 and 153 for H_2O/CO_2 and H_2O/SO_2, respectively. With the overall conditions improving on August 2, we calculated a plume speed of 1.1 to 3.9 m s^{-1}, resulting in a H_2O flux between 29,862 ± 16,723 t d^{-1} using the measured H_2O concentration of 25,350 ppm. This resulted in a SO_2 flux of 694 ± 701 t d^{-1} and a CO_2 flux of 6,758 ± 5,525 t d^{-1} using the Multi-GAS average ratios of 10.8 and 153, respectively. On this day, the artifacts of the images were caused by vignetting due to the camera position towards the incident light and some possible lens misalignments, described in a similar spectroscopic instrument for NO_2 detection by Kuhn et al., (2022).

3.2.3 miniDOAS

We collected miniDOAS data (Table 3) obtained by walking and car traverses. We estimated a plume width of between 100 and 400 m by walking traverses and of up to 1 km by car traverses approximately 8 km downwind from the vent. IMO wind data (Supplementary Material Table S1) was used to calculate the standard deviation averages for wind speeds and directions to obtain the SO_2 emissions variability. The presented value was calculated with data obtained by our field measurements and detailed in Table 3. Additionally, we used our measured Multi-GAS data averages (Table 1) to calculate the H_2O and CO_2 emissions by multiplying the SO_2 fluxes obtained from miniDOAS with the corresponding gas ratios. For the days of July 14 to July 28 we used the Multi-GAS H_2O/SO_2 ratio of 72.2 ± 62.1 and a CO_2/SO_2 ratio of 5.4 ± 2.7. Afterwards, we used a Multi-GAS H_2O/SO_2 ratio of 153.0 ± 68.8 and 5.7 ±2.8. which are the average measurements for August 2.

On July 14, we measured an SO_2 flux of 6,506 ± 1,922 t d^{-1} by car traverse, resulting in a calculated H_2O flux of 132,088 ± 152,632 t d^{-1} and a CO_2 flux of 24,134 ± 19,197 t d^{-1}. On July 21 the SO_2 emissions dramatically decreased, to 459 ± 121 t d^{-1}, obtained by walking traverse. This flux yields a H_2O flux of 9,319 ± 10,472 t d^{-1} and a CO_2 flux of 1,703 ± 1,300 t d^{-1}. On July 22, we measured an SO_2 flux of 441 ± 223 t d^{-1} by walking traverse yielding a H_2O flux of 8,953 ± 12,228 t d^{-1} and a CO_2 flux of 1,636 ± 1,645 t d^{-1}.

https://doi.org/10.5194/egusphere-2025-6430
Preprint. Discussion started: 29 January 2026

On July 24 we measured an SO_2 of 352 ± 94 t d^{-1} by walking traverse. However, spectral saturation occurred during these measurements, making the data unreliable. Despite this limitation, we calculated a H_2O flux of 7,146 ± 8,055 t d^{-1} and a CO_2 flux of 1,306 ± 1,002 t d^{-1}. On July 25, we measured an SO_2 flux of 692 ± 70 t d^{-1} by walking traverse and calculate a H_2O flux of 14,049 ± 13,505-t d^{-1} and 2,567 ± 1,543t d^{-1} CO_2 flux.

On July 28 we made a car traverse, which had spectral saturation. Despite this, we measured an SO_2 flux of 516 ± 567 t d^{-1}, which corresponds to a calculated H_2O flux of 10,476 ± 20,522t d^{-1} and a CO_2 flux of 2,020 ± 3,230 t d^{-1}. On August 1, we performed a car traverse and measured an SO_2 flux of 466 ± 114 t d^{-1} and calculated a H_2O flux 20,049 ± 13,914 t d^{-1} and a CO_2 flux of 1,825 ± 1,336t d^{-1}. On August 2 we made another car traverse resulting in a SO_2 flux of 394 ±224 t d^{-1} with calculated H_2O flux of 16,994 ± 17,274t d^{-1} and a 1,547 ± 1,631 t d^{-1} of CO_2 flux.

3.2.4 UV Camera

UV camera images were collected on July 28 and August 2, 2023 (Table 4). July 28, we were unable to obtain a good linear fit for the calibrated points, which suggests that the calibration was not properly performed. Fig 9 B shows the calibration with the linear trend and processed images. With this in mind we calculate a plume speed of 4.1 m s^{-1}, giving us a value of 47 ± 33 t d^{-1} SO_2 flux, On August 2, we obtain a good calibration fit, and we calculate a plume speed of 4.1 ms^{-1} and a total flux of 118 ± 45 t d^{-1} SO_2, The calculated fluxes of H2O and CO2 based on these measurements and corresponding Multi-Gas measurements are summarized in Table 4.

https://doi.org/10.5194/egusphere-2025-6430
Preprint. Discussion started: 29 January 2026

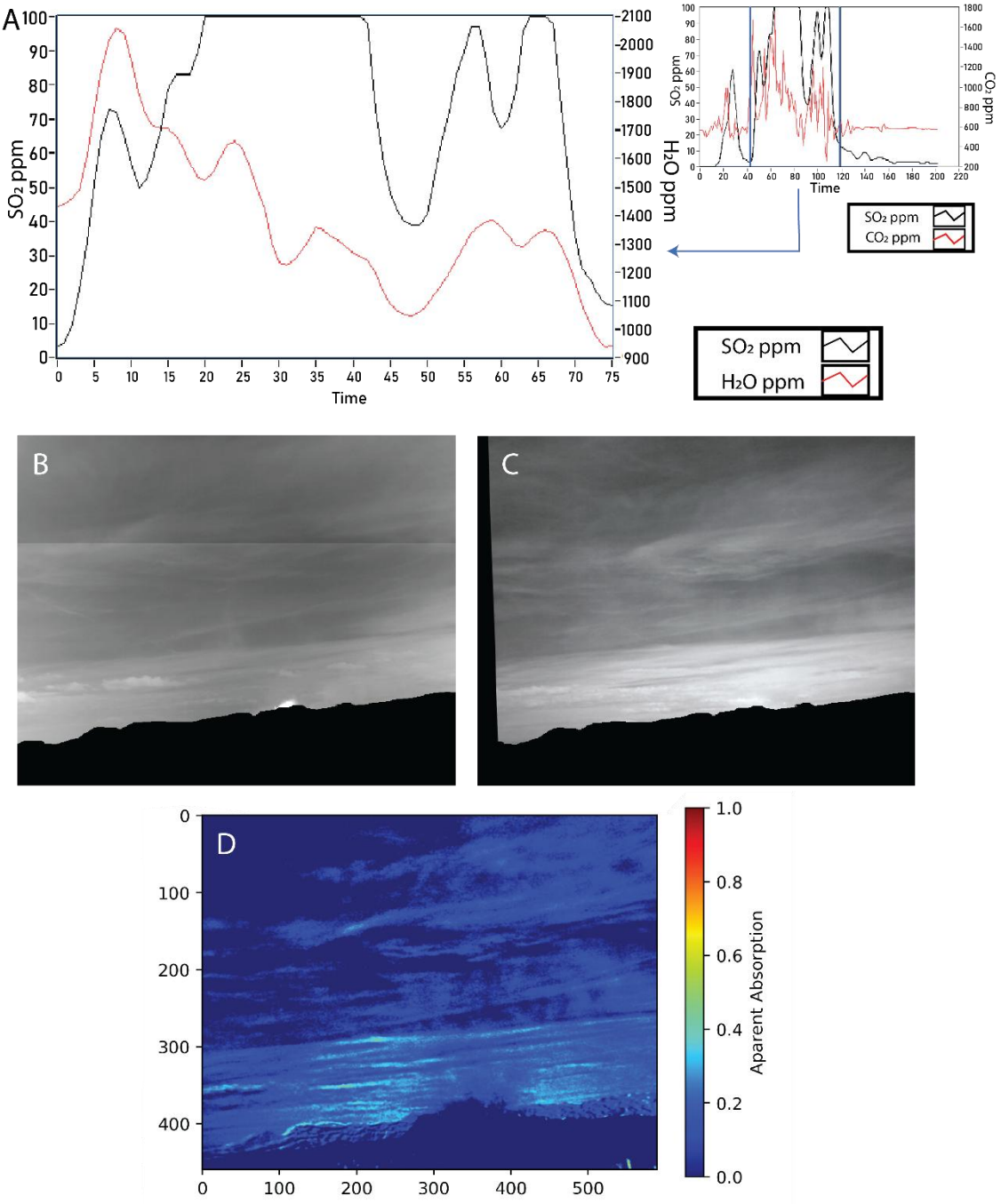

Figure 11 A) Sample data displaying SO_2 and the H_2O converted from RH% to ppmv using the temperature and the pressure of 980 hPa for Iceland sea level pressure from our sensors using Ratiocalc 3.2 (Tamburello 2014) The right inlet shows the selected region from a SO_2/CO_2 graph as an example. B-D) Images from Litli Hrútur on 28 July 2023. B and C are images taken with the camera instrument for lenses 850 and 940 nm, respectively. The images are corrected, masked, and aligned. D The processed image using the method of Beer-Lambert with water droplets correction using the visible (VIS) image. The light tones in the color image show the H_2O as apparent absorption.

https://doi.org/10.5194/egusphere-2025-6430
Preprint. Discussion started: 29 January 2026

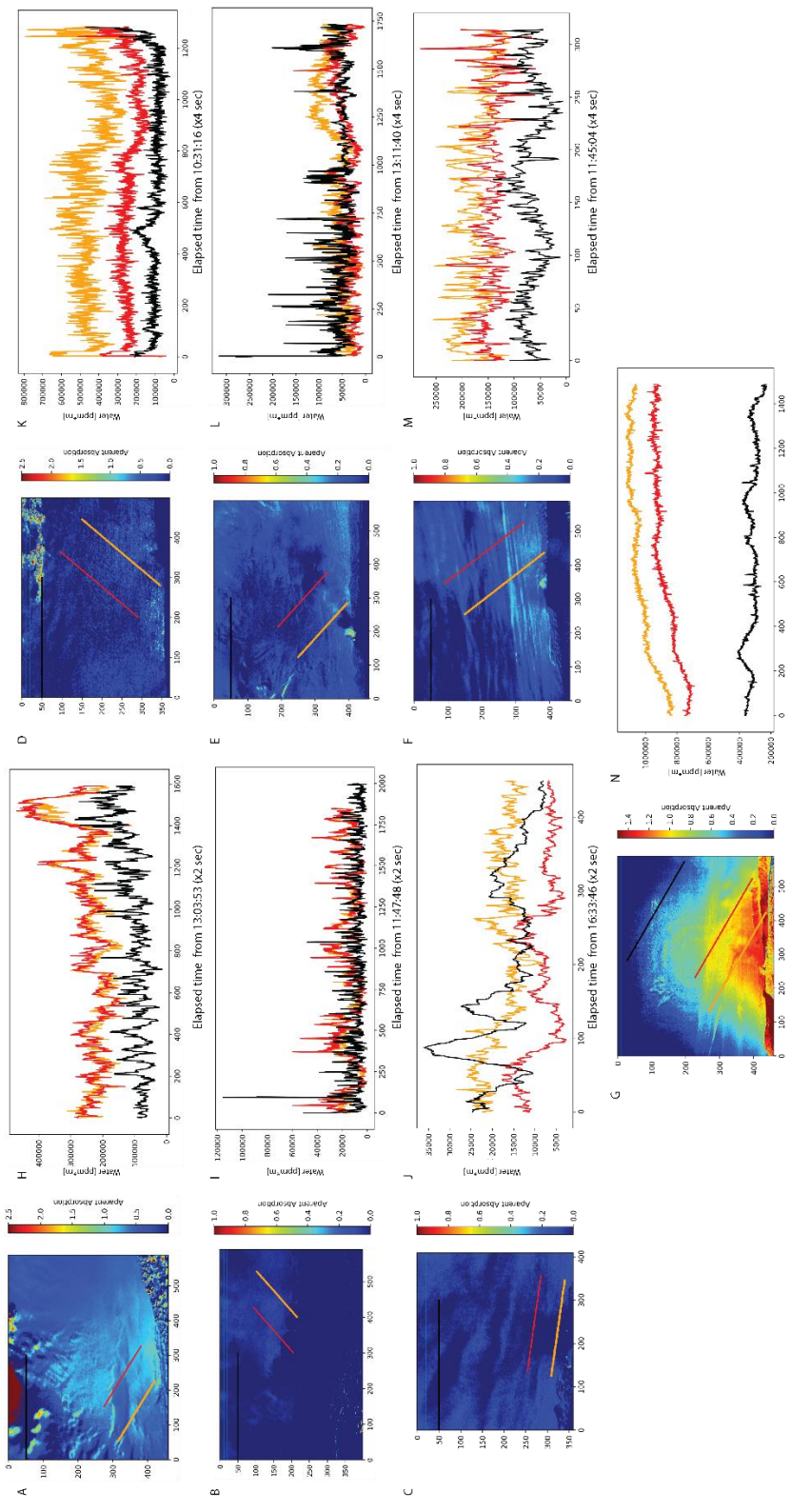

Figure 12 A-G, Processed images with the drawn column amounts near the vent (orange), also used as plume width, a displaced line far from the vent (red) for wind estimation using cross-correlation, and a farther away line to show the background (Black). The Images show apparent absorbance after using the Beer-Lambert law and corrected with the VIS image H-N) Corresponding cross-correlation. In orange is the near vent starting amount, Red is the subsequent amount, black is drawn in a background region. The H_2O vapor concentration lowers with distance from the source and with elevation, and both near(orange), and far (red) are similar and different from the background (black), this is consistent with the scale height of water vapor. Additionally, supplementary representative videos of each valid sequence are available.

520 **Table 1 Multi-Gas data for Lascar and Litli Hrútur presented as molar ratios. In red a sample is shown with possible moss contamination while sampling. * Ground based Multi-GAS measurement.**

Volcano	Date	Max Temperature	Max H_2O	H_2O/SO_2		H_2O/CO_2		CO_2/SO_2	
	[DD/MM/YYYY]	[°C]	[ppm]		±		±		±
Lascar	13-10-2022+*	18.5	7,264	-	-	19.1	6.7	-	-
	13-10-2022+*	11.0	7,264	-	-	1150.8	654.1	-	-
	12-11-2022+*	27.0	19,816	253.8	186.5	-	-	-	-
	26-11-2022*	18.0	10,600	-	-	-	-	-	-
	26-11-2022*	15.5	13,000	86.5	26.8	-	-	-	-
	29-12-2024*	38.5	21,551	-	-	-	-	-	-
Litli Hrútur	21-07-2023	37.0	21,700	-	-	41.3	23.9	-	-
	24-07-2023	60.6	49,503	-	-	17.0	17.1	-	-
	25-07-2023	25.0	-	-	-	-	-	-	-
	27-07-2023	26.0	18,503	72.2	62.1	5.9	5.6	5.4	2.7
	28-07-2023	62.0	30,200	-	-	199.6	115.1	-	-
	02-08-2023	66.0	34,892	137.2	94.3	11.7	11.0	6.3	2.9
	02-08-2023	71.0	35,155	168.7	43.2	9.9	9.3	5.1	2.7
	02-08-2023	53.0	21,000	124.5	130.3	13.7	8.4	23.3	16.5

. - not calculated

+ Ckelar Data

Note 1: For reference Talabre measured 23.3°C for temperature and 18% relative humidity at 3300m asl. corresponding to H_2O = 3.75 g/m^3 or 7,718 ppmv, which corresponds to a pressure of 5.17 hPa.

Note 2: For Reference Litli Hrútur area had a temperature of 13°C and ~60% humidity at 200m asl. corresponding to H_2O = 7.16 g/m3 or 9,646 ppmv, which corresponds to a pressure of 9.45 hPa

525 **Table 2. Summary of the processed image data for Lascar and Litli Hrútur. In red are unreliable processed data due to unfavorable atmospheric conditions or calculated plume speed error >60%. The calculated plume speeds were obtained from the camera measurements. * calculated plume speeds (anemometer) obtained with hand-held anemometer data over the Integrated Column Amounts.**

Volcano	Day [DD/MM/YYYY]	Latitude	Longitude	Altitude [m a.s.l.]	Distance from crater [km]	Frequency of picture [s]	Total Images/ filter	Calculated Plume speed (anemometer)* [m/s]
Lascar	**26-11-2022**	-23.367	-67.7314	5478	0	1	1530	-
	27-11-2022	-23.327	-67.7314	3895	7.94	1	571	7.90-20.3
	27-11-2022	-23.327	-67.7314	3895	7.94	1	392	-
	28-11-2022	-23.314	-67.7314	3240	17.21	3	80	-
	28-11-2022	-23.314	-67.7314	3240	17.21	3	130	-
	30-11-2022	-23.313	-67.7669	4160	6.2	4	328	4.76-13.8
	30-11-2022	-23.313	-67.7669	4160	6.2	4	176	4.19-12.1
	29-12-2025	-23.403	-67.7169	4160	4.3	1	2760	3.15-7.39 (5.0-10.0)
	29-12-2025	-23.403	-67.7169	4160	4.3	1	3302	3.00-17.2 (6.0-14.0)
Litli Hrutur	**19-07-2023**	63.9182	-22.2126	220	0.45	4	2413	13.67-14.75
	21-07-2023	63.92	-22.21	220	0.45	2	2228	27.1 (7-9.1)*
	22-07-2023	63.9182	-22.2126	220	0.45	2	458	.- (5)
	24-07-2023	63.92	-22.21	220	0.45	4	2768	1.36-5.28- (3.3-4.23)*
	25-07-2023	63.9182	-22.2126	220	0.45	4	2485	.-(3)*
	27-07-2023	63.92	-22.21	220	0.45	4	1926	3 (2.7-4.2)*
	28-07-2023	63.92	-22.21	220	0.45	4	323	.- (4.2-5.6)*
	02-08-2023	63.92	-22.21	220	0.45	4	1496	1.10-3.90 (1.8-2.7)

530 **Table 2 continued**

Volcano	Date	Average H_2O flux		ppm conversion	Multi-GAS ratios		Calc. SO_2 flux		Calc. CO_2 flux	
	[DD/MM/YYYY]	[t/d]	± [t/d]		H_2O/CO_2	H_2O/SO_2	[t/d]	± [t/d]	[t/d]	± [t/d]
Lascar	**26-11-2022**	-	-	13,000	-	-	-	-	-	-
	27-11-2022	34,787	15,283	13,000	19.1	86.5	1,430	1,071	4,449	3,515
	27-11-2022	-	-	13,000	-	-	-	-	-	-
	28-11-2022	-	-	13,000	-	-	-	-	-	-
	28-11-2022	-	-	13,000	-	-	-	-	-	-
	30-11-2022	12,143	5,914	13,000	19.1	86.5	499	398	1,553	1,301
	30-11-2022	22,415	10,884	13,000	19.1	86.5	922	753	2,867	2,398
	29-12-2025	46,891	18,863	21,155	19.1	86.5	1,928	1,373	5,997	4,516
	29-12-2025	112,968	79,479	21,155	19.1	86.5	4,644	4,707	14,449	15,234
Litli Hrutur	**19-07-2023**	20,291	771	13,600	17.0	72.2	999	898	2,916	3,044
	21-07-2023	-	-	13,600	-	-	-	-	-	-
	22-07-2023	-	-	6,000	-	-	-	-	-	-
	24-07-2023	20,094	11,862	49,503	17.0	72.2	990	1,436	2,887	4,609
	25-07-2023	2,065	-	-	5.9	72.2	4	3	855	806
	27-07-2023	2,919*	635*	18,503	5.9	72.2	144	155	1,209	1,402
	28-07-2023	6,185*	884*	30,200	10.8	153.0	144	85	1,400	560
	02-08-2023	29,862	16,723	25,350	10.8	153.0	694	701	6,758	5,525

535 **Table 3 Average reported values from Lascar Volcano from OVDAS-SERNAGEOMIN, Chile. (data available at https://rnvv.sernageomin.cl/volcan-lascar/) and average miniDOAS for SO_2 estimated data with measured wind speed and wind directions in the field with anemometer for the Litli Hrútur eruption. In red are shown the values for a saturated spectrum, which are considered invalid measurements. nd is non determined parameter.**

Volcano	Date	SO_2 concen-tration	plume width	Field wind speed	field wind direction	average SO_2 flux		Multi-GAS		Calc. H_2O flux		Calc. CO_2 flux	
	[DD/MM/YYYY]	[ppm*m]	[m]	[m/s]		[t/d]	± [t/d]	H_2O/ SO_2	CO_2/ SO_2	[t/d]	± [t/d]	[t/d]	± [t/d]
Lascar	**10-01-2022**	nd	nd	nd	nd	764	47	86.5	19.0	18,583	6,901	9,972	4,130
	11-01-2022	nd	nd	nd	nd	424	46	86.5	19.0	10,313	4,314	5,534	2,552
	12-01-2022	nd	nd	nd	nd	285	46	86.5	19.0	6,934	3,268	3,267	1,912
	01-01-2023	nd	nd	nd	nd	483	74	86.5	19.0	11,752	5,442	6,304	3,189
	25-12-2024	nd	nd	nd	nd	293	63	86.5	19.0	7,126	3,740	3,824	2,171
Litli Hrútur	**14-07-2023**	1,475	831	17	10	6,506	1,922	72.2	5.4	132,088	152,632	25,028	19,197
	21-07-2023	3,000	67	7	330	459	121	72.2	5.4	9,319	10,472	1,768	1,300
	22-07-2023	1,200	363	3.9	275	441	223	72.2	5.4	8,953	12,228	1,695	1,645
	24-07-2023	3,000	172	4.3	30	352	94	72.2	5.4	7,146	8,055	1,393	1,002
	25-07-2023	2,850	149	5.2	310	692	70	72.2	5.4	14,049	13,505	2,642	1,543
	28-07-2023	350	1209	6.7	30	516	567	72.2	5.4	10,476	20,522	1,984	3,060
	01-08-2023	250	350	3	350	466	114	153	5.7	20,049	13,914	2,247	1,336
	02-08-2023	275	767	2.7	30	395	224	153	5.7	16,994	17,274	1,516	1,631

Table 4 Summary for UV camera data from Lascar volcano, provided by Ckelar research group, and calculated data for Litli Hrútur.

Volcano	Date	latitude	longitude	distance from crater	plume speed	SO_2 flux		Multi-GAS		Calculated H_2O flux		Calculated CO_2 flux	
	[MM-DD-YYYY]			[km]	[m/s]	[t/d]	± [t/d]	H_2O/SO_2	CO_2/SO_2	[t/d]	± [t/d]	[t/d]	± [t/d]
Lascar	27-01-2022	-23.30829	-67.75896	4.2	7.9	338	115	86.5	19.0	8,217	5,341	4,409	3,703
	28-01-2022	-23.30829	-67.75896	6.6	8.1	903	100	86.5	19.0	21963	9,235	11,785	4,283
	31-05-2022	-23.39322	-67.72444	2.9	14.3	105	4	86.5	19.0	2,542	884	1,364	345
Litli Hrútur	28-07-2023	63.9182	-22.2126	0.45	4.1	47	33	153	5.6	2,007	2,335	180	212
	02-08-2023	63.9182	-22.2126	0.45	6.4	118	45	153	5.6	5,055	4,228	452	402

https://doi.org/10.5194/egusphere-2025-6430
Preprint. Discussion started: 29 January 2026

4 Discussion

4.1 Measurement approach, performance, limitations, and potential

4.1.1 Water vapor absorption, NIR detection, sensitivity and optimal conditions

The significant difference in the atmospheric air temperature, pressure, and relative humidity compared to the plume allows for transporting excess H_2O over several hundred meters from the source. Fig 6 and equation 1 demonstrate the strong vapor saturation pressure dependance on temperature, implicitly affected by pressure, which allow an air parcel to hold more H_2O molecules, increasing by a factor of ~10 every 30°C. Additionally, if the relative humidity in the atmosphere is low compared the plume (like Lascar), the plume H_2O content could be 5 to 50 times larger than background. These conditions enable our system to detect H_2O from the passive degassing Lascar and the Litli Hrútur eruption. In fact, if we were measuring just humidity variation under the same conditions it would likely be challenging as previously reported by Kern (2017) comment on Pering et al., (2017).We further corroborate this principle with the HITRAN radiative transfer simulations (Rothman et al., 2012) using similar and slightly higher atmospheric parameters from both field sites as explained in the Methods section and in the Appendix Figures A1 and A2). The model confirms the differential absorption ability of the 940 nm and 850 nm filters, which shows absorption in the arid, high-altitude site and in the humid, sea level conditions. Therefore, our approach expands its applicability beyond what was previously reported (Kern 2017, Kern et al., 2017; Kern et al., 2025).

At both sites, we observed an important increase in plume H_2O concentration relative to background. At Lascar the plume concentration reached 21,155 ppm versus 7,718 ppm of H_2O of the background obtained at Talabre. Similarly, at Litli Hrútur, we observe 49,503 ppm H_2O in the plume versus the background values of 9,646 ppm H_2O.

The H_2O content differences are mainly driven by the temperature contrast between plume and ambient air, with a 10-30 °C difference at Lascar (this work; Gaete et al., 2015; Lopez et al.,2015). If we consider the air at Talabre town as background, there is up to 0.5% difference in weight of H_2O between the air measured at Talabre and the plume on November 26, 2022, equivalent to 2.6 hPa under these conditions. The difference is ~5 hPa on December 29, 2024, differences in H_2O molecules between the plume and the background create favorable conditions for H_2O detection (Kern et al., 2017). The same is true for the Litli Hrútur eruption because of the higher temperature of the gases emitted from the erupting lava fountains. In this case, our UAV-based Multi-GAS measurements show a sharp increase in temperature (up to 71°C) tens of meters above the active crater. This temperature increase is the result of erupted lava temperatures of ~1000 -1190 °C based on thermal camera estimates (Bruce Houghton pers. comm) and glass composition (https://jardvis.hi.is/is/efnasamsetning-kviku-gossins-vid-litla-hrut-11-juli-2023). Therefore, as long as the temperature in the center of the plume remains higher and relatively stable, the number of H_2O molecules will also be higher in the plume center than in the surrounding atmosphere even in high humidity conditions (40-70% RH), with condensation occurring at the border of the plume.

https://doi.org/10.5194/egusphere-2025-6430
Preprint. Discussion started: 29 January 2026

For our case, it is true that the sensitivity threshold would depend on the atmospheric background and plume temperature contrast. However, the NIR system shows a quantifiable signal in this infrared region, previously noted as difficult to detect with low-grade instruments (Kern et al., 2017; Platt et al., 2018). This method is shown to be sensitive to water vapor in the atmospheric column, but that sensitivity is highly dependent upon atmospheric conditions. It is evident that if an optically opaque plume of white scattering water droplets is visibly apparent, then our method would not detect the vapor phase H_2O (Fig 12 B,C, and E). Hence, significant errors occur due to light path changes by aerosol scattering, if these conditions are not met. For a UV-based SO_2 camera system, Kern et al. (2010) showed that these errors can exceed 70%.

Alternatively, if the atmosphere is visibly clear and there is no apparent scattering, then our method should be predominantly sensitive to the water vapor (Fig 9 and Fig 12 A, D, F, and G). Furthermore, at both sites, the plume's translucent appearance shows that the condensation was not efficient (Fig 10 and Fig 15b and black lines in Fig 12 and Fig 8) and showed the expected decrease in H_2O towards the top of the image (Fig 12 K, F and N panels).

4.1.2 Novel capabilities and performance

This study represents the first successful deployment of light scattering NIR cameras to quantify volcanic H_2O flux at a passively degassing arc volcano (Lascar, Chile) where traditional OP-FTIR techniques would be challenging, and in a sea-level, humid environment (Litli Hrútur, Iceland). We simultaneously deployed both the UV and NIR camera at the Litli Hrútur, 2023 eruption, demonstrating for the first time, that volatile emissions are not necessarily mixed within the plume. This was observed at times when the high gas content with one system was also detected as a lower emission with the other system, in other words, the puffs of SO_2 detected by the UV camera are seen as "shadows" by the NIR camera. Conversely, when puffs of H_2O are present in the field of view of the NIR camera, they show up as shadows in the UV camera system (Fig 13, supplementary videos of similar timeframes, and drawn on Fig 9 for UV camera).

A similar observation with an FTIR system was made for the Fagradalsfjall 2021 eruption by Scott et al., (2023). Additionally, Pfeffer et al., (2024) reported plume heights and SO_2 emissions during a different eruption at the same volcano in 2021, which show low SO_2 emission rates with high plumes (up to 4,000 m), implying that during these periods, gases other than SO_2 , possibly H_2O and CO_2, are sustaining the eruption,. The simultaneous observations with both UV camera and NIR camera have the potential to determine fluxes and H_2O/SO_2 ratios in real-time to assess short-term fluctuations due to volcanic activity and plume-atmosphere interactions.

Although these two systems were not deployed simultaneously at Lascar, the same pattern of shadows within the plume are drawn on Fig 9. Similar high and low H_2O concentrations are observed in the NIR camera sequences. We show the most obvious puffs in the supplementary video for December 29, 2024. ,

https://doi.org/10.5194/egusphere-2025-6430
Preprint. Discussion started: 29 January 2026

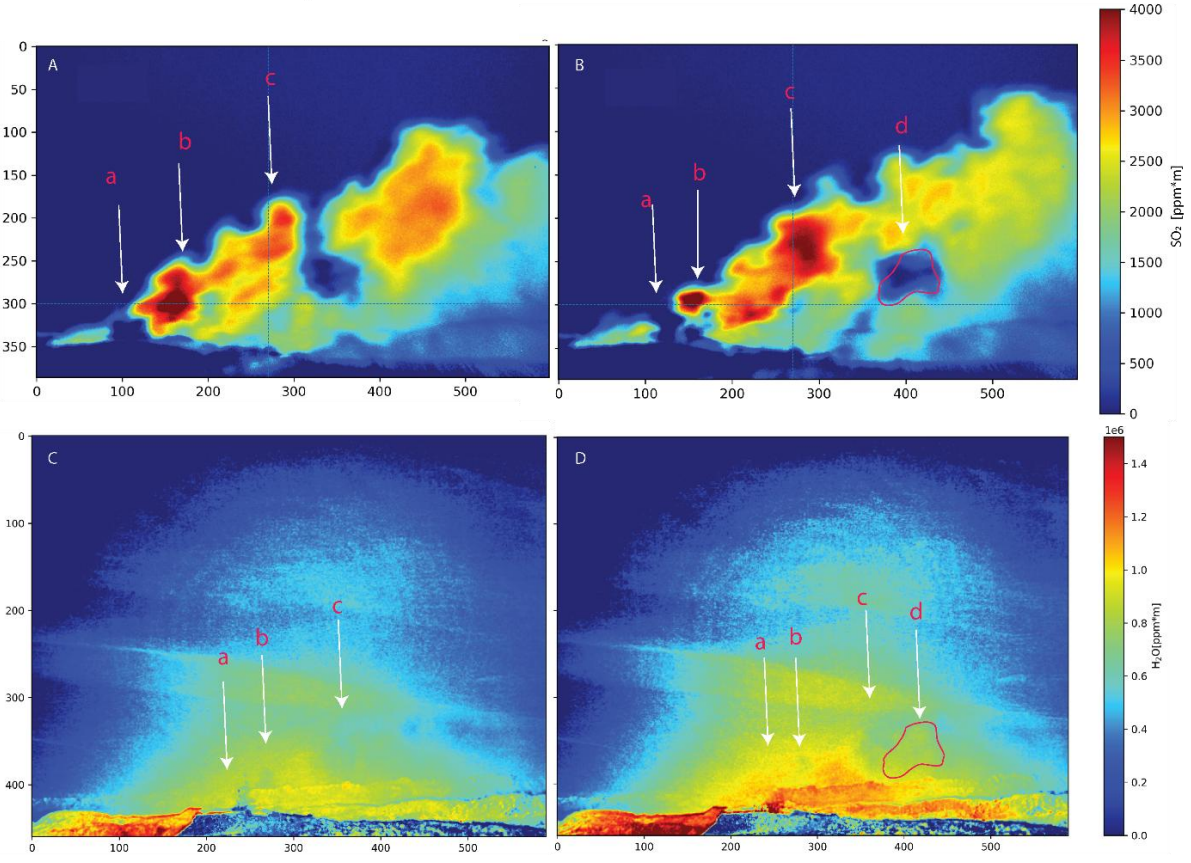

Figure 13 Consecutive images (A-B) from the UV camera and (C-D) from the NIR camera sequences, taken simultaneously with the same timestamp. The arrows indicate differences in absorbance detected by each system. The corresponding absorbance shadows are visible in images A and C, and B and D, respectively. The arrows with lowercase letters point to a similar location in both images to help identify these shadows, and a shape is drawn which shows great resemblance on the UV camera system.

Our plume speed measurements obtained using the cross correlation technique with NIR camera system also align with the wind speed calculated using the independent llano Chajnantor data near Lascar, with the anemometer data (Table 2), and IMO data (Supplementary Material Table S1) for Iceland. From those values, the standard deviation of the average plume and wind speed difference between the NIR camera cross-correlation technique and the anemometer is + 0.5-1.4 m s^{-1} for Lascar and + 4.3 for Litliu Hrútur. We see a difference between the calculated cross-correlation method using the UV camera that estimated 6.4 m s^{-1} on August 2, 2023, this is 3 m s^{-1} higher than the wind speeds obtained by anemometer and NIR cross-correlation. We attribute this discrepancy to the difference in the acquisition times between these techniques.

Nevertheless, local volcanic morphology and geography settings must also be considered. Lascar's deep crater and topography generate localized eddies, causing plume velocities to diverge from expected values and often do not agree with meteorological measurements. We see this issue in the second sequence of December 29, 2023, where gas moves slower and stalls. Further future work is needed with various techniques deployed exactly at the same time to improve the critical parameter of volcanic plume speed for complex site-specific conditions.

https://doi.org/10.5194/egusphere-2025-6430
Preprint. Discussion started: 29 January 2026

4.1.1 Limitations and future improvements

Potential sources of error in plume gas detection using UV cameras have been identified by Lübcke et al., (2014) and include light interaction with particles such as aerosol, droplets or ash as well as mie scattering. Our NIR camera system only accounts for first order aerosol correction, with further normalization using a visible wavelength image. Under favorable measurement conditions, including an ash-free plume, a clear sky, <5 km from the plume, and a >10 °C difference between plume and air, we estimate the error of the NIR camera system to measure H_2O to be similar to that of an UV camera and about ± 20-30% (Lübcke et al., 2014). Under unfavorable conditions, these errors propagate more intensively in the NIR camera, and we estimate an error to ± 70%. This limitation for the NIR camera system was seen at both Lascar (November 27, 2022 and the second sequence on December 29, 2024) and Litli Hrútur (July 21, 22, 25 and 27, 2023).

The high noise in the images from Lascar can be explained by technical factors and the inability to choose a lower near horizon background in the north of Chile. The noise could be potentially corrected by applying a similar method to Kuhn et al., (2024), that uses a polynomial fit of the entire background,. We can further eliminate the aerosols error in Lascar region because they were at a minimum according to the radiometer at llano Chajnantor (available at https://www.apex-telescope.org/apex-dashboard/d/MQgvc4Onz/historical-weather?orgId=1&var-year=2022&var-month=11) and have long been low in this region (Aguilera et al., 2022). We also exclude the effect of snow and rocks causing scattering towards our cameras because we did not observe intense reflection in the field. However, we did experience a high infrared absorbance of insects, which could induce transitory errors (Fig. 14 A and B).

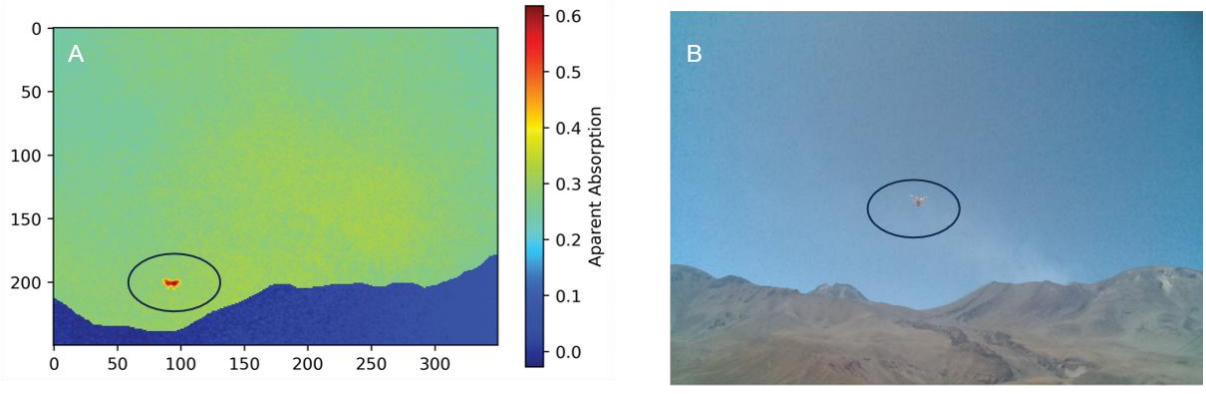

Figure 14 These images show one of the challenges when acquiring pictures and correlating images in the post-process. A) shows a single bug with the high scattering noise produced by bugs. which is also what is seen by the VIS sensor in B.

A current limitation of the NIR camera system is the need for measuring the relative humidity and temperature of the plume independently using an in-situ sensor system. This data is used to obtain water vapor concentration in the plume, which is used to calibrate the NIR images' apparent absorption. In most cases this can be achieved by flying a humidity sensor into the plume using a UAV. Alternatively, for continuous monitoring, data from a permanent Multi-GAS and meteorological stations system could be used accounting for varying conditions or having a calibrated thermal camera paired with lookup tables to derive humidity values and then calculate the water emissions.

https://doi.org/10.5194/egusphere-2025-6430
Preprint. Discussion started: 29 January 2026

4.2 Lascar emissions

Lascar volcano shows persistent passive degassing throughout the year with a wide variation in SO_2 emissions over the past two decades. The reported SO_2 fluxes range from ~200 to >2400 t d^{-1} (Wilkes et al., 2023; Bucarey et al., 2020; Lopez et al., 2015; Menard et al., 2014, Tamburello et al., 2014, Henney et al., 2012; Mather et al., 2004). Such fluctuations are characteristic of the volcano's cyclic degassing behavior and fluid motions, which has also been documented by Gaete et al., (2020) for the 2015 eruptive period and by radiance variations in Layana et al., (2020) for a period between 1984-2019. Figure 16 shows the H_2O, CO_2, and SO_2 fluxes obtained from all the instruments used in this study and literature values reported from past years. The NIR camera measurements used the Multi-GAS field data (Table 1) for H_2O/SO_2 and H_2O/CO_2 ratios of 86.5 ± 26.8 and 19.1 ± 6.7, respectively. These ratios are in agreement with direct sampling method used by Tassi et al., (2009) with 3.02-95.3 for H_2O/SO_2 and within the range of 0.31-22.5 H_2O/CO_2 for samples collected above 100°C. We used the Tassi et al., (2009) CO_2/SO_2 ratio of 19.0 and H_2O/SO_2 ratio of 54 to extrapolate literature data when not provided.

In November 2022, the emissions of SO_2 reported by OVDAS-SERNAGEOMIN (Fig 16 and Table 3) were becoming consistently lower, reaching a minimum of 285 t d^{-1} SO_2, approaching the eruption on December 8, 2022. During this period, the reports (available online under Reporte de Actividad Volcánica—RAV, December 2022) show an increase in plume height suggesting elevated heat and gas flux. This apparent contradiction can be explained by an overall higher water emission at this time, as observed in the field and with our NIR camera system with a daily average emission of 23,115 ± 10,694 t d^{-1} H_2O for November data. These average H_2O emissions are four times higher than the H_2O flux reported by Tamburello et al., (2014) of 5,192 t d^{-1} derived using Multi-GAS H_2O/SO_2 ratio and SO_2 flux from a field campaign in 2012. Additionally, the Multi-GAS derived SO_2 fluxes from the NIR gives reasonable values between 950 ± 440 t d^{-1} SO_2 with levels concordant with those reported by OVDAS-SERNAGEOMIN of 1,031 t d^{-1} SO_2 (available online under Reporte de Actividad Volcánica—RAV, November 2022) differing just slightly from miniDOAS measurements. Since the uncertainties are still relatively high, all measurements could benefit from having multiple independent techniques running simultaneously to elucidate the individual spatial-temporal variations of H_2O, CO_2, and SO_2 emissions.

Regarding using our H_2O measurements to elucidate the eruptive processes, we can attribute the 2022 vulcanian eruption (Global Volcanism Program, 2022) to two possible mechanisms; the one proposed by Gaete et al., (2020) which suggests over-pressurization of the volcanic system due to the infiltration of meteoric water and rapid vaporization due to hot volcanic rocks, causing a phreatic event. The higher H_2O fluxes (with a low magmatic component) captured by our measurements would explain a more buoyant plume and dilution of the SO_2 in the plume and hence the lower SO_2 flux reported by OVDAS-SERNAGEOMIN, a phenomenon also mentioned for Sabancaya by Kern et al., (2017). The other theory, in which the puffs that we see in our sequences (Supplementary Videos November 2022 and December 2024) also lend credence to magmatic convection cells proposed by Layana et al., (2020) inducing a cyclic gas emission. High variability in fluids is also seen by Tassi et al., (2009) and explained as a reflection of the high hydrothermal interaction of the volcano. It could also be attributed to persistent magma movement, a mechanism that contributed to magma mixing causing the 1986-1994 eruptive process

https://doi.org/10.5194/egusphere-2025-6430
Preprint. Discussion started: 29 January 2026

(Stechern et al., 2024). We think that coupling our H_2O camera system with the UV camera will further help to elucidate these physical processes. The interplay between H_2O and SO_2 gases provides key information for eruption forecasting (i.e. Stix and de Moor, 2018).

At the time of our measurements, Lascar's emissions showed variations similar to those seen by Menard et al., (2014). Throughout this period of persistent degassing, we were able to distinguish "puffs" of emissions (Fig 16) with maximum flux average of 50,084 ± 22,003 t d^{-1} of H_2O. Puff emissions have also been observed and described for SO_2 gas in Menard et al., (2014) and variations from 20.8 to 34.7kg s^{-1} SO_2 (or 1,800-3,000 t d^{-1} SO_2) have been reported by Mather et al., (2004).

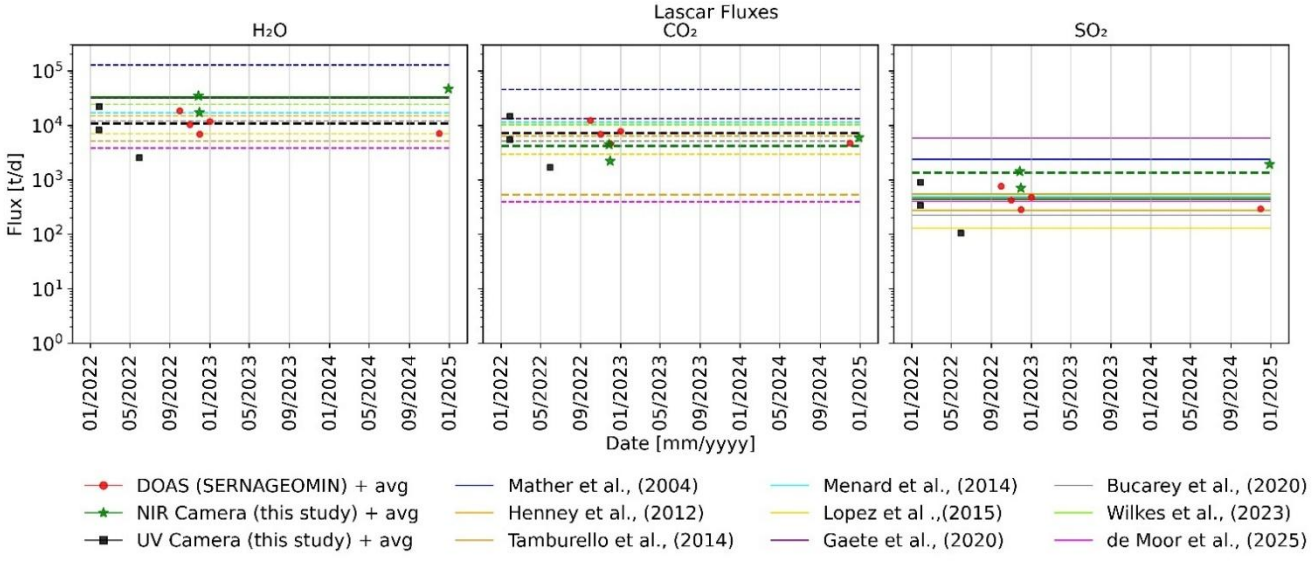

Figure 15 Log scale plot summarizing Lascar volcano measurement using DOAS (dark red circles), NIR (Green stars), and UV camera (Black squares), and Literature averages. The H_2O, CO_2, and SO_2 fluxes averages are represented with lines, which are grouped by gas, colored by author, and indicated by dash lines if they were derived from Multi-GAS/in-situ data, or continuous line if they were obtained directly. We extrapolated when needed using Tassi et al., (2009) in-situ measurement ratios of 54 H_2O/SO_2 and 23 $CO_2/SO2$.

Nonetheless, using our approach under ideal conditions, H_2O significantly exceeds the atmospheric background levels, and we were able to obtain average H_2O fluxes of 29,059 ± 12736 t d^{-1} for all the valid data from the passively degassing Lascar volcano. At Lascar these high H_2O emissions are likely due to the hydrothermal system's input of minor and constant water vapor to the plume. It is important to note that Tassi et al., (2009) observed great variability in H_2O contents of emitted gases for different fumaroles, which is typical for most volcanic systems (Fischer 2008; Fischer and Chiodini 2015). In fact, the exit temperature is one of the indicating parameters for H_2O origin and great variability inside Lascar Crater (Ai et al., 2023). For hydrothermal sourced fumaroles, the exit temperature is much lower than that of the magmatic ones (Tassi et al., 2009). This mingling of multiple water content fumaroles into one observed plume is relevant for our measurements because plumes emitted from high temperature vents can retain more heat allowing H_2O to be visible with our NIR camera system for longer

https://doi.org/10.5194/egusphere-2025-6430
Preprint. Discussion started: 29 January 2026

distances before equilibrating with the atmosphere. The supplementary videos also show discrete plumes traveling upwards or getting mixed inside of the crater, a usual pattern for Lascar due to the crater size and wind variations.

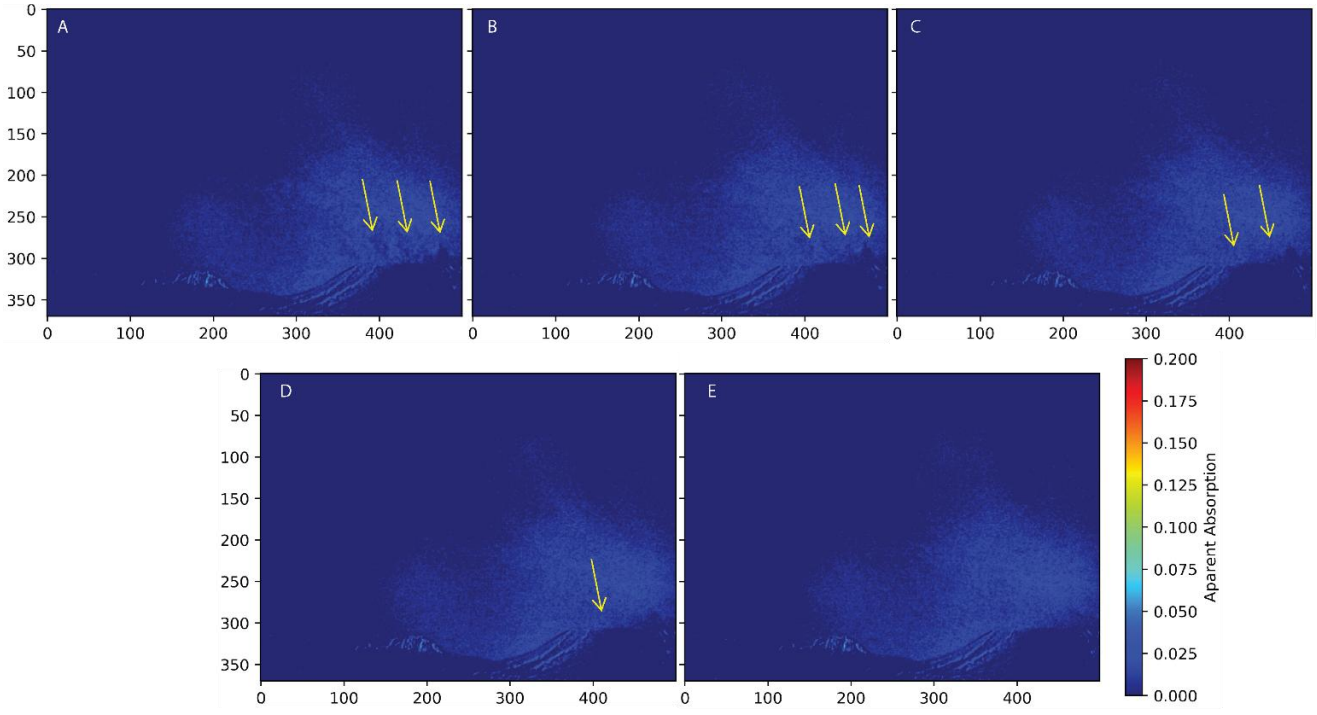

Figure 16 The sequence of images from A - E show the movement of water vapor and the background atmosphere. The background does not prevent the detection of higher concentrations of water vapor in the plume as puffs dispersing int eh atmosphere are clearly seen as they travel away from the volcano. (full video with Supplementary material).

4.3 Litli Hrútur eruption

We present a comprehensive report of volcanic gases emitted from 2023 Fagradalsfjall event, complementing the recent study by Fischer et al., (2024) that measured CO_2 flux and $\delta^{13}C$ throughout the 2023 Litli Hrútur eruption indicating extensive isotope fractionation. Similarly to the previous section, Fig 17 compares our values to averages fluxes of H_2O, SO_2, and CO_2 for different techniques and reported values. Notably, Fig 17 shows an apparent inverse relationship between miniDOAS and NIR camera values that align well with the observations of increased activity during July 25, which elevated the SO_2 values for a few days to then steadily decrease until August 5 to a progressively more condensed and lowered temperature plume. The increase in emissions is also seen in satellite SO_2 instruments during July 24-26 (https://so2.gsfc.nasa.gov). Though it is different in size and time, we plotted 2021 reported gas data for reference.

Multi-GAS ratios measured during the eruption show $CO_2/SO_2 = 5.6\pm2.8$, $H_2O/SO_2 = 126.0\pm66.5$, and $H_2O/CO_2 = 11.1\pm10.7$. The CO_2/SO_2 ratio is slightly elevated compared to Fischer et al. (2024) at 3.0, while H_2O/SO_2 exceeds parallel IMO OP-FTIR measurements. The H_2O/CO_2 ratio agrees well with IMO data, although the high variability (±10.7) could be caused by moss fire contributions and lava outgassing. The main discrepancy in SO_2 measurements may have been measurements distant from

https://doi.org/10.5194/egusphere-2025-6430
Preprint. Discussion started: 29 January 2026

the plume with a greater contribution of emissions from outgassing lava which is therefore SO_2 poor. Another possibility that adds to the previous one is the natural decrease in SO_2 towards the end of the eruption, which would increase the H_2O/SO_2 ratios.

Comparing our average NIR-derived SO_2 flux value (440 ± 174 t d^{-1} SO_2) to that obtained by miniDOAS traverses (1,493 t d^{-1} SO_2) we see this deficit in observed SO_2. The deficit in SO_2 is even more pronounced by the UV camera averages (82 t d^{-1} SO_2). However, if we consider only similar days of measurements, without July 14 when the eruption started, the average values are much closer to miniDOAS traverses at 490 ± 150 t d^{-1} SO_2 flux. Nonetheless, a decline in SO_2 flux towards the end of an eruption, coupled with the decreased sensitivity of UV spectrometers as the season moves towards winter, emphasizes how important it is to have alternative methods to monitor volcanic emissions that are not SO_2 and UV dependent. The UV camera under detection of SO_2 is possibly due the lower light conditions, low zenith angle, and camera positioning (viewing angle) showcasing that in Iceland these measurements are always difficult. Another possible explanation for the discrepancy between these techniques is that our calibration was not fully performed under SO_2 clean sky.

Troll et al., (2024) proposed a crustal level accumulation zone that continuously fed Fagradalsfjall volcano from 2021 to Litli Hrútur 2023 and continuing with the Sundhnúkur Fires in 2024. If there is a connected system then the reported petrologically-derived H_2O estimates should be similar and give insight to our estimates. Pairing this assumption with the lava effusion rate of 9 m s^{-1} from IMO (https://en.vedur.is/about-imo/news/earthquake-activity-in-fagradalsfjall-area; Thordarson et al., 2023), and a rock density of 2,600 kg m^{-3} (Scott et al., 2023), we can use Radu et al., (2023) measured pre-eruptive magmatic water content from clinopyroxene data (~0.75% H_2O average), which yields 175.5 kg s^{-1} H_2O (15,163 t d^{-1} H_2O). Similarly, Halldorsson et al., (2022) gives 51.5 kg s^{-1} H_2O (4,448 t d^{-1} H_2O) using partially degassed melt inclusion data (~0.22% wt.% H_2O). Additionally, Radu et al. (2023) estimates that 74-94% of initial magmatic water was lost during degassing. Furthermore, by the end of Litli Hrútur 2023 eruption, plume carbon isotopes indicate a mostly degassed magma (Fischer et al., 2024; Moussallam et al., 2024), which would make surface gas emissions even more dominated by H_2O. This is consistent with our NIR instrument H_2O fluxes (19,108 ± 7,560 t d^{-1} H_2O) and the SO_2-derived estimates of 13,873 ± 13,479 t d^{-1} H_2O (though with high uncertainty). These observations, however, cannot confirm the single-reservoir system (Troll et al., 2024), but they are consistent with a progressive degassing path where H_2O will increasingly dominate at lower pressures due its pressure-solubility dependance.

Nonetheless, similar to Lascar volcano emissions, identifing shallow meteoric processes contributing to plume H_2O content, which is a perennial source of uncertainty in volcanic plume/magmatic processes studies, needs to be addressed, and our camera system offers an approachfor this. Pairing these systems with other instruments (i.e. Multi-GAS, FTIR) to derive additional gas emission rates has the caveat that we are assuming no spatial or temporal variability, which is not the case as shown on Fig. 13. For future events, it would be ideal to have a consistent and integrated techniques to estimate daily emissions of multiple gases directly and independently from dedicated instruments.

https://doi.org/10.5194/egusphere-2025-6430
Preprint. Discussion started: 29 January 2026

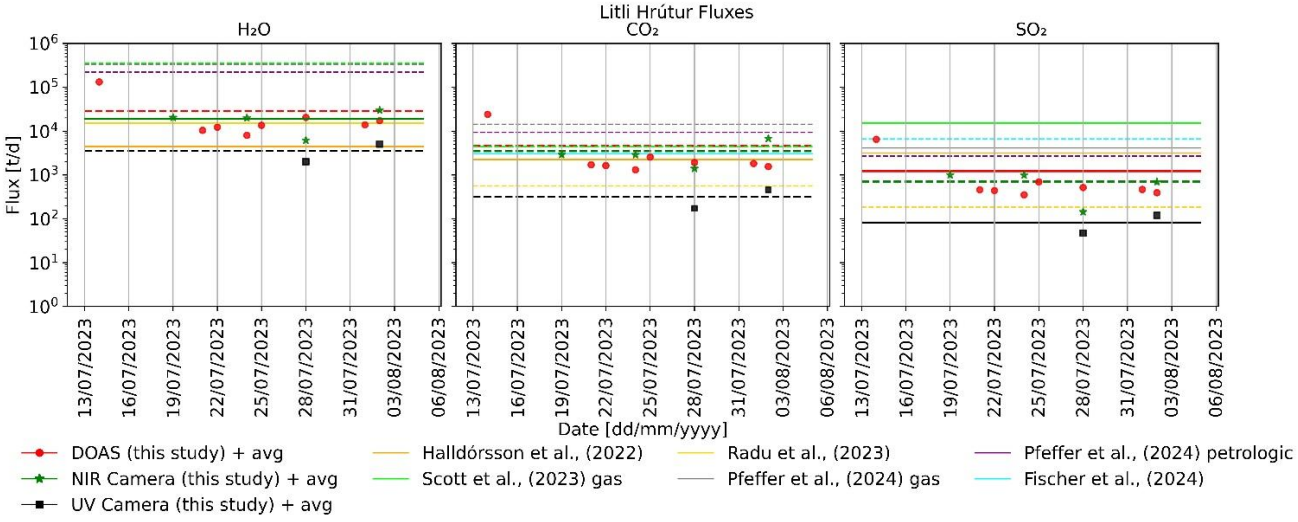

Figure 17: Log scale plot summarizing Litli Hrútur eruption measurement using miniDOAS (red circles), NIR camera (Green stars), UV camera (Black squares). For reference, literature averages are shown. The H_2O, CO_2, and SO_2 fluxes averages of are represented with lines, which are grouped by gas, colored by author, and indicated by dash lines if they were derived from Multi-GAS/in-situ data, or continuous line if they were obtained directly. We calculated the missing literature gases by using Scott et al., (2023) FTIR average ratios of 81.6 for H_2O/SO_2 and 3.48 for CO_2/SO_2.

4.4 Eruptive and global water vapor fluxes

For the Fagradalsfjall volcano, we extrapolated the average measured values from the NIR camera, the miniDOAS, and the UV camera (Table 5) for the 23 days of the Litli Hrútur eruption. The NIR/Multi-GAS emissions, show 0.016 Tg of SO_2, while miniDOAS measured 0.034 Tg of SO_2 . The latter are possibly skewed by the high emissions of July 14. In both cases the values are 5 times higher than the average of the data retrieved from satellites a discrepancy that has been observed previously in Icelandic SO_2 measurements (Esse et al., 2023).

For H_2O, we see a similar pattern, the NIR camera system shows an average of 0.44 Tg of H_2O emission for the eruption. , The miniDOAS/Multi-GAS method shows an average at 0.77 Tg H_2O. Using the average 11.1 H_2O/CO_2 Multi-GAS ratio and the average flux of 35 kg s^{-1} (20-50 kg s-1) from Fischer et al., (2024) the extrapolated value is 0.77 Tg H_2O emitted during the eruption. This could represent the highest bound for the H_2O emission, due to the gas being sampled closer to the most active period of the eruption for both Fischer et al, (2024) and our first miniDOAS/Multi-GAS measurement. Comparing these values to literature estimates, we see that the closest values to the ones presented are the ones constrained by petrologic analysis of Radu et al., (2023) and Halldórsson et al., (2022), with the caveat that these estimates come from a different eruption event in 2021.

Table 5 Emission rate compilation from literature and this study for Lascar (yearly), Litli Hrútur (eruption duration), CVZA (yearly using 21 volcanoes with fumarole activity) and global arc (yearly using 168 degassing sources around the world). In bold are data obtained directly from an instrument (i.e. DOAS for SO_2), italic shows fluxes derived from SO_2 flux or H_2O flux combined with Multi-GAS ratios, underlined means obtained from petrologic studies.

https://doi.org/10.5194/egusphere-2025-6430
Preprint. Discussion started: 29 January 2026

Lascar Fluxes

Reference	H_2O (Tg/yr)	SO_2 (Tg/yr)	CO_2 (Tg/yr)
Mather et al., (2004)	*20.1*	**0.88**	*14.15*
Henney et al., (2012)	*1.54*	*0.10*	*1.32*
Menard et al., (2014)	*2.77*	**0.18**	*2.38*
Tamburello et al., (2014)	*1.90*	**0.20**	**0.19**
Lopez et al., (2015)	*2.55*	**0.05**	0.62
Kern et al., (2017)*	***91.3***	*3.98*	*11.44*
Gaete et al., (2020)	*3.2*	**0.21**	2.78
Gaete et al., (2020) eruption avg.	*29.2*	**0.89**	*1.31*
Bucarey et al., (2020)	*1.25*	**0.08**	*1.08*
Wilkes et al., (2023)	*2.49*	**0.16**	*2.14*
de Moor et al., (2025)	*1.41*	**0.15**	*0.15*
This study Average	**10.6**[1]	3.99[2] 3.98[3]	0.46[1] **0.164**[2] 0.164[3]	*1.36*[1] 2.14[2] 2.14[3]

Litli Hrútur eruption fluxes

Reference	H_2O (Tg)	SO_2 (Tg)	CO_2 (Tg)
Scott et al., (2023)	*2.33*	**0.10**	*0.352*
Halldórsson et al., (2022)	*0.102*	**0.072**	*0.052*
Radu et al., (2023)	*0.349*	*0.004*	*0.013*
Pfeffer et al., (2024)	*2.17*	**0.095**	*0.329*
Pfeffer et al., (2024)	*1.41*	**0.062**	*0.214*
Fischer et al., (2024)	*0.317*	**0.152**	**0.070**
This study Average	**0.439**[1] 0.772[2] 0.081[3]	0.016[1] **0.034**[2] 0.002[3]	*0.080*[1] 0.128[2] 0.007[3]

CVZA fluxes

Reference	Average type	H_2O (Tg/yr)	SO_2 (Tg/yr)	CO_2 (Tg/yr)
Hilton et al., (2002)	Total Andean Arc	242.12	3.03	11.83
Fischer (2008)	Total Andean Arc	*76.20*	**3.03**	*13.77*
Tamburello et al., (2014)	Total CVZA	*10.00*	**0.67**	*0.69*
de Moor et al., (2025)	Total CVZA	*13.87*	**2.37**	*0.92*
This study Average*	Total CVZA	**222**[1] *83.9*[2] *83.6*[3]	*9.16*[1] **3.45**[2] *3.44*[3]	*28.5*[1] *45.0*[2] *44.9*[3]

Global Fluxes

Reference	H_2O (Tg/yr)	SO_2 (Tg/yr)	CO_2 (Tg/yr)
Hilton et al., (2002)	1,460	20.2	63.8
Wallace(2005)	300	10.0	100
Fischer (2008)	*653*	**20.2**	85.0

https://doi.org/10.5194/egusphere-2025-6430
Preprint. Discussion started: 29 January 2026

Fischer et al., (2019)		*30.3*			**7.81**			*6.43*	
Kelley and Fischer (2025)		486			27.3			52.8	
This study average**	**1,780**[1]	670[2]	669[3]	**73.3**[1]	27.6[2]	27.5[3]	227.9[1]	360[2]	359[3]

Considering the above, the total emissions of H_2O, SO_2, and CO_2 during the 23 days duration of the Litli Hrútur eruption of 0.544 Tg is a conservative number of the total gas emission, although it benefits from the consideration that H_2O, SO_2, and CO_2 are directly measured. These are the first calculated water vapor emissions from the Fagradalsfjall fires, where most of the eruptions have no reports on H_2O flux data and represent 1.5 times the average described in Fischer et al., (2019) and Werner et al., (2019) for Plume settings.

Over that past four decades, global fluxes of water vapor and other gases have been constrained using the traditional method of COSPEC/miniDOAS or satellite-based DOAS fluxes combined with gas ratios obtained by direct sampling or Multi-GAS (e.g. Williams et al., 1992; Fischer et al., 1998; Fischer, 2008, Burton et al., 2013; Aiuppa et al., 2019; Fischer et al., 2019; Werner et al., 2019) or using petrologic approaches combined with magma emplacement rates (summarized in Wallace 2005; Kelley and Fischer, 2025). As mentioned before, while generally valid for obtaining average emission rates, the approaches have the disadvantage that each gas emission rate is ultimately dependent on the measured SO_2 emission and does not allow one to individually obtain the fluxes of the gas of interest. For the petrologic method, wide variations in magma emplacement rate estimates, especially for some arcs, make results uncertain (Kelly and Fischer, 2025). Using our approach, we show that for Lascar and the Litli Hrútur eruption, H_2O and other gas emission rates may vary significantly over time, potentially independent of or inversely with SO_2 flux. To compare our result with regional and global estimates, we compiled the emission rates from literature for Lascar volcano, Litli Hrútur eruption, the Central Volcanic Zone of the Andes (CVZA), and global estimates in Table 5.

The CVZA values were calculated assuming that Lascar is representative of this portion of the arc. We used 21 volcanoes that show fumarolic activity, out of the 62 recognized active volcanoes (Aguilera et al., 2022). For the global arc system, we used 168 out of 540 volcanoes, that is 40.3 Tg out of the 53 Tg, or 76% of the total global emissions (Fischer et al., 2019). In these cases, assuming our NIR camera H_2O fluxes averages of Lascar (10.6 Tg yr^{-1}) are representative of water emissions, that would already be 1/3 of the total fluxes calculated by Fischer et al., (2019) of 1,680 x 10^9 mol yr^{-1} (or 30 Tg yr^{-1}) of magmatic H_2O emitted from volcanoes in South America. Fischer (2008) presented a similar compilation based on SO_2 data showing estimates of 4.23 x 10^{12} mol yr^{-1} (or 76 Tg yr^{-})[1] of H_2O degassing from Andean volcanoes, in this case, if we use Lascar average emission for 21 active volcanoes, we would get 223 Tg yr^{-1} of H_2O with our NIR camera and 83.9 Tg yr^{-1} with DOAS/Multi-GAS ratio, the latter being close to averages proposed by Fischer (2008), and the NIR camera values closer to the ones proposed by Hilton et al., (2002) for the total Andean arc (242 Tg yr^{-1}). Tamburello et al., (2014) using SO_2 flux and Multi-GAS ratio calculated 10 Tg of H_2O, and a recent compilation of the CVZA by de Moor et al., (2025) show magmatic H_2O emissions of 13.3 Tg yr^{-1}. All these values are closer to the minimum average measured values with our NIR camera, however, for the higher end,

https://doi.org/10.5194/egusphere-2025-6430
Preprint. Discussion started: 29 January 2026

Kern et al., (2017) is the only H_2O targeted flux study in this region, with measured values of 250,000 t d^{-1} (or 91.3 Tg yr^{-1}) at Sabancaya in 2016, even higher than the Lascar emission rate. An important remark is that Kern et al., (2017) measured these values while the volcano was active, which probably had more thermal energy that contributed to hydrothermal waters being evaporated, and are drastically different to the 2,698 t d^{-1} (0.9 Tg yr^{-1}) measured by Moussallam et al., (2017) using miniDOAS/UV camera paired with H_2O/SO_2 Multi-GAS ratios. In our case it is also likely that high hydrothermal (low temperature) gas flux was the cause for higher water contribution closer to the eruptive period in December 2022 and may be the cause for the high noise in December 2024. This highlights the important contribution of this gas to the atmosphere with 10 times more emissions than when passively degassing. Additionally, the comparisons in Table 5 show how the miniDOAS/UV cameras are dependent on the H_2O/SO_2 Multi-GAS ratios.

In terms of global emissions Hilton et al. (2002) report a global water flux of 1,440 Tg yr^{-1} H_2O (or 8 x 10^{13} mol yr^{-1}), significantly higher than the flux reported by Wallace (2005) based on MI data and magma emplacement rates of 300 Tg yr^{-1}. Recently, a compilation from Kelley and Fischer (2025) MI based ranges have estimated ~486 Tg yr^{-1} (2.7 x 10^{13} mol yr^{-1}) of H_2O for global arc volcanoes. Using the 168 most contributing volcanoes from Fischer et al., (2019) and our measurements of Lascar as the average, we get 1,782 Tg yr^{-1}, a value close to the estimates of Hilton et al., (2002), though if we were to use the miniDOAS/Multi-GAS, we would be in the vicinity of the values of Kelly and Fischer (2025) and Wallace (2005). Additionally, if we consider the SO_2 fluxes values in Table 5, we see that NIR camera/Multi-GAS SO_2 are about 2 times the SO_2 values. Therefore, these examples illustrate that either SO_2 flux rates used in global calculations are underestimated (this is unlikely because they are consistent between satellite and ground-based methods (Fischer et al., 2019) or that H_2O/SO_2 ratios used in these calculations are too low. Another possibility is that the Lascar and Sabancaya water emissions include a significant meteoric water component that skews the fluxes to higher values. Future work on δD and $\delta^{18}O$ measurements of plumes could address this issue.

5 Conclusions

We presented the first simultaneously deployed NIR camera, UV camera, and DOAS measurements in contrasting sites. The passively degassing high altitude and arid atmosphere Lascar (Chile), and the actively erupting, sea-level and humid atmosphere Litli Hrútur 2023 eruption (Fagradalsfjall, Iceland), demonstrating that H_2O and SO_2 vary independently over time. This is essential considering that other gases fluxes have been estimated based on SO_2 emissions and constant volatile/SO_2 ratios. Our approach allows us to identify and quantify water in the plume independently, using scattering light and varying atmospheric conditions, and performs best in clear-sky conditions, <6 km distance from the source, and when plume atmosphere temperatura contrast is high (>10°C).

For Lascar volcano, the average H_2O fluxes (~29,000 ± ~13,000 t d^{-1}) show five times higher values than previous SO_2-derived measurements, and with clear recognition of H_2O puff emissions. At Litli Hrútur eruption 2023, NIR camera-derived fluxes (~19,000 ± ~7,600 t·d^{-1}) agree with petrological estimates of past eruptions, especially considering the degassed magma at the

https://doi.org/10.5194/egusphere-2025-6430
Preprint. Discussion started: 29 January 2026

moment of measurement, which validates the approach. For the 23 days of eruption, we estimated a total eruptive emission of 0.544 Tg of total volatile emission, with 439 kt of H_2O, 34.3 kt of SO_2, and between 80.2-128 (NIR-derived vs DOAS-derived) kt of CO_2. Notably, we distinguish a continuous decline of SO_2 and a clear increase in H_2O values observed toward the end of the eruption, consistent with magma degassing models and the carbon isotope data.

In both locations, Lascar and Litli Hrútur 2023, the NIR camera instrument enabled direct, near-real time H_2O flux measurements, difficult to obtain with other instruments. More importantly, the simultaneous NIR camera and UV camera simultaneous deployment revealed that H_2O and SO_2 puff emissions are often spatially decoupled within the plume suggesting that traditional SO_2-based extrapolations fail to capture the short-term H_2O variability, with clear implications for volatile budgets.

Although this system is limited to favorable and stable atmospheric conditions to consistently obtain fluxes and avoid irregularities caused by light dispersion or scattering, the NIR camera represents a step forward in volcanic gas measurements and understanding volcanic gas emission dynamics. This approach can provide important information for hard to access situations where direct gas sampling or in-situ gas sensing is not possible and where significant variations in gas fluxes are expected or observed. This paper emphasizes the need for continuous and simultaneous instrument deployment and data acquisition to understand the evolution of individual gas species and advance the distinction between hydrothermal and magmatic gas contributions using remote sensing techniques. Such data could be a significant step towards eruption forecasting and advancing the dynamic and variable emissions of volcanic gases into the atmosphere. Direct H_2O flux measurements at more volcanoes globally will likely put better constraints on global volcanic water emissions and the deep-water geochemical cycle.

Appendix A: HITRAN plume simulation

We used HITRAN database (Rothman et al., 2013) to simulate atmospheric transmission and absorption scenarios to support the field observations obtain using the Near Infrared Camera. All the calculations were performed using the HAPI (HITRAN API) Python library.

The simulations were conducted over the 900-980 nm spectral range with a resolution of ~0.01 cm^{-1} per line due to the main absorption band for H_2O and our camera system. Additionally, we simulated a Light source (LED) spectrum similar to what is described in Kern (2017). We modelled the LED using a Gaussian curve centered at 940 nm ± 10 nm , this is less than our camera filter response of 940 ± 20 nm.

We considered 3 scenarios of water vapor (H_2O), assuming the gas is diluted in air: (1) the background without spectral broadening for H_2O, (2) the plume with a spectral broadening coefficient of 0.2, and (3) an extreme case with a broadening coefficient of 0.3 caused by H_2O. Additionally, we use 2 methods to calculate the total relative radiance, one directly using the HITRAN internal calculations (Appendix Fig A1), which allows to obtain transmissivity for background and plume. These are then multiplied to obtain the total transmissivity for which the optical depths and radiance after passing through a bandpass filter can be calculated. The other method (Appendix Fig A2) was calculated by obtaining the amounts of water vapor

https://doi.org/10.5194/egusphere-2025-6430
Preprint. Discussion started: 29 January 2026

molecules given the specific conditions for the plume and background and fix path lengths for each case, this was then used to obtain the optical depths and radiance behind a bandpass filter.

For Iceland the atmospheric background parameters were set to 15 °C at 55% Relative humidity (RH) and a pressure of 1013.25 hPa. Plume conditions were simulated at 90 °C, 90% RH, and the extreme case was calculated for 99 °C and 99% RH, both cases under the same pressure as background.

For Lascar, the atmospheric background parameters were 10 °C at 10% RH and a pressure of 560 hPa. Plume conditions were simulated at 35°C, 70% RH, and an extreme case using 65 °C, 90% RH, also at 560 hPa.

All simulations assumed negligible scattering. For Lascar, we represented different background path lengths set to 0.5, 2, 5 and 10 km with a simulated plume thickness of 200 and 400 m based on the Lascar crater size (~600 m). For Iceland, we simulated background path length of 0.5 and 2 km, with simulated plume thickness of 40 and 100m (based on the crater and plume size). These values are agreement with field observations as well as passive volcanic emissions (Harris and Ripepe, 2007).

Figure A1. HITRAN simulations of relative radiance obtained from Transmissivity for Lascar, Chile. The calculations were done using the internal HAPI calculations (HITRAN_units=False) to directly obtain Transmissivity. In this setup, the path length has to be provided (fixed).
For Lascar, we used A-B 0.5 km atmosphere, C-D 2 km atmosphere, E-F 5 km atmosphere, and G-H 10 km atmosphere. The atmospheric background (black lines) were calculated at 560hPa (~4,600 m asl) pressure at a temperature of 10 °C 10%RH. The plume normal and extream case (blue and red lines, respectively) were model with 35 °C-70%RH and 65 °C-90%RH with left figures showing a 200m plume thickness and the right a 400m plume.
For Fagradalsfjall, we used I-J 0.5km atmosphere, K-L 2km atmosphere 1013.25hPa (sea level) pressure at a temperature of 15 °C 55%RH. The plume normal and extream case (blue and red) were model with 90 °C-90%RH and 99 °C-99%RH with left figures showing a 40m plume thickness and the right a 100m plume.
These simulations illustrate the change in relative radiance as the light pass through simulated volcanic plumes is on varying background atmospheric with fix path lengths.

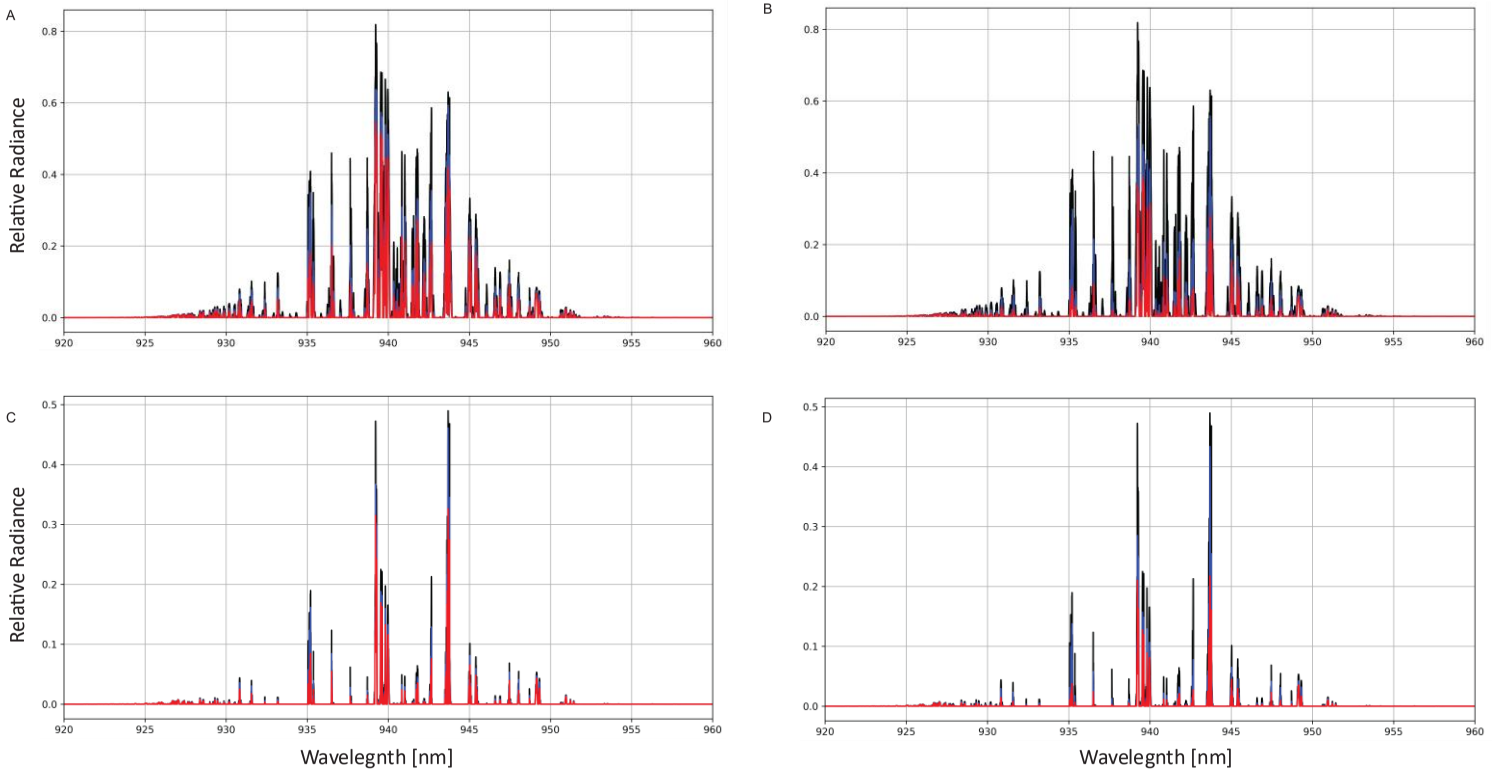

Figure A1 Continue

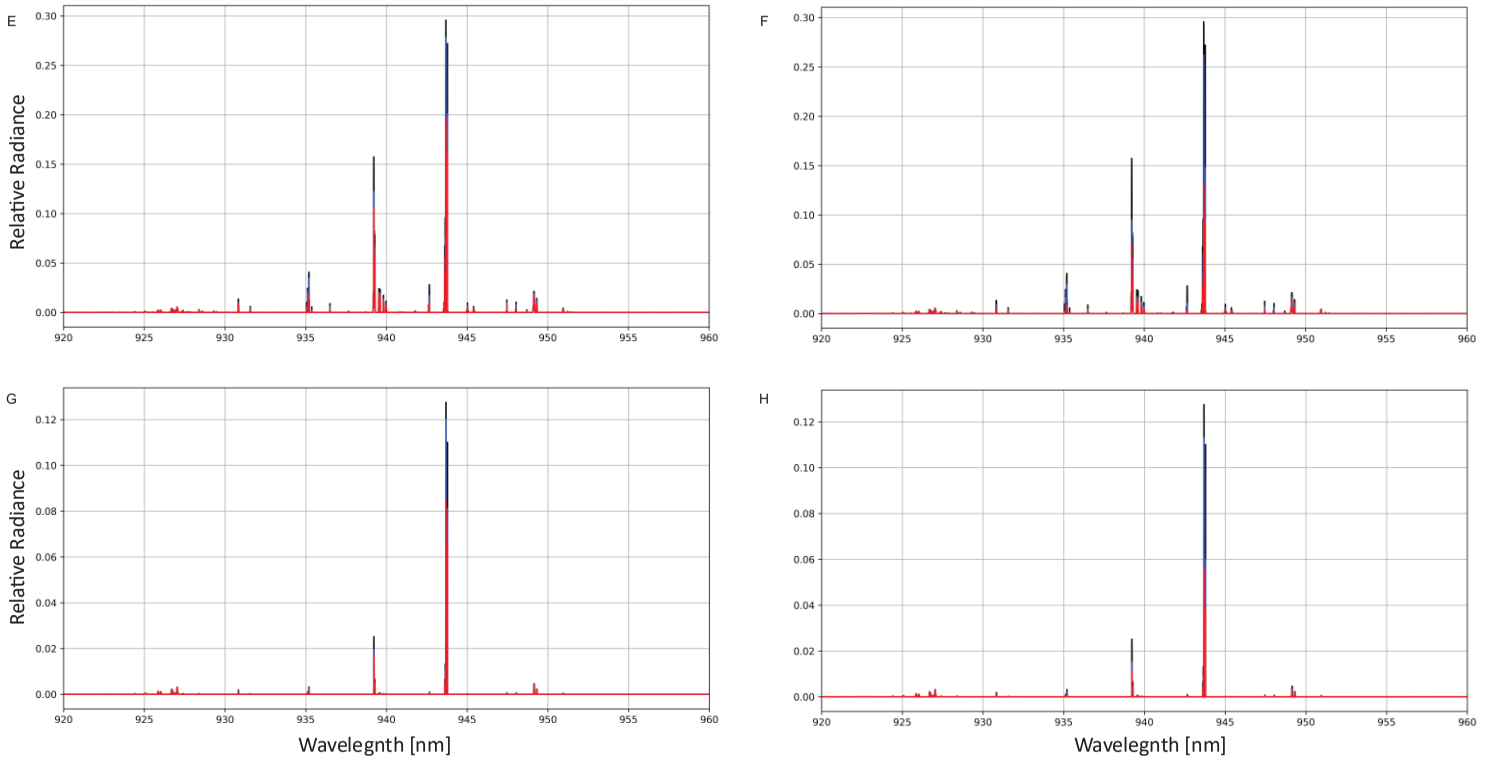

895

https://doi.org/10.5194/egusphere-2025-6430
Preprint. Discussion started: 29 January 2026

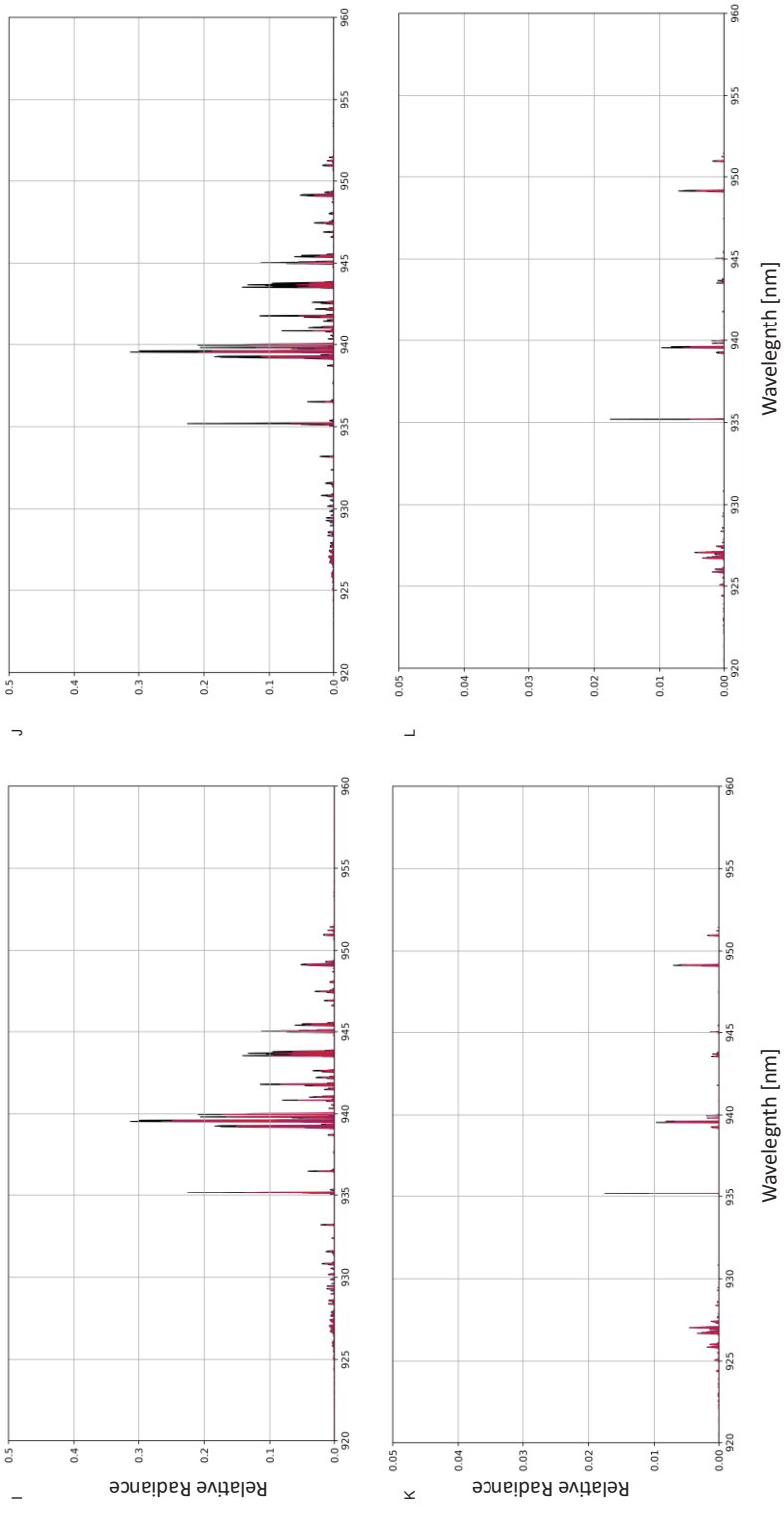

Figure A1 Continue

https://doi.org/10.5194/egusphere-2025-6430
Preprint. Discussion started: 29 January 2026

Figure A2 HITRAN simulations of relative radiance behind a bandpass filter obtained from Lascar, Chile and Fagradalsfjall, Iceland. The calculations were done using the internal HAPI calculations (HITRAN_units=True) to directly obtain absorption cross sections (cm^2/molecules) given specific conditions. The optical depths (τ) are obtained by taking the negative logarithm from Beer Lambert Law. A-C represent Lascar simulations calculated using 560 hPa (~4,600 m asl) air temperature-Relative humidity of of 10 °C-15% RH, plume temperature of 35 °C-70% RH, and a plume extream case of 65 °C-90% RH. The differences in these figures are in the camera FOV angles at 10, 20 and 40°. They show a 30% (up to 53%) more absorption when the plume is in the path. D-F represent Lascar simulations calculated using 640 hPa (~3,600 m asl) for the same atmospheric and plume parameters. 44% (up to 55%) more absorption. G (active soruce)-J represent Fagradalfjall sumulations calculated using 1013.25hPa 40 m plume and atmospheric parameters of 15 °C-55% RH and a plume of 90 °C-90%and an extream case of 99 °C-99%. For H, I and J the differences are in the viewing angle of 10, 20 and 40 °. In these cases the background absorption is much higher than the plume, though in direct path (G) the plume and background have a 12% difference in water vapor absorption, enough to be quantified even at 40% filter efficiency. For each figure, the pink area we represent the initial light intensity from a band pass filter centered at 940nm ±20nm, blue is the light after passing through the atmosphere with a scale height of 2km, and in red and black are the 2 cases of light passing through the plume without background. The aparent absorptions were calculated based on scattered light formulation highlighted in Kern (2017) and active source for G.

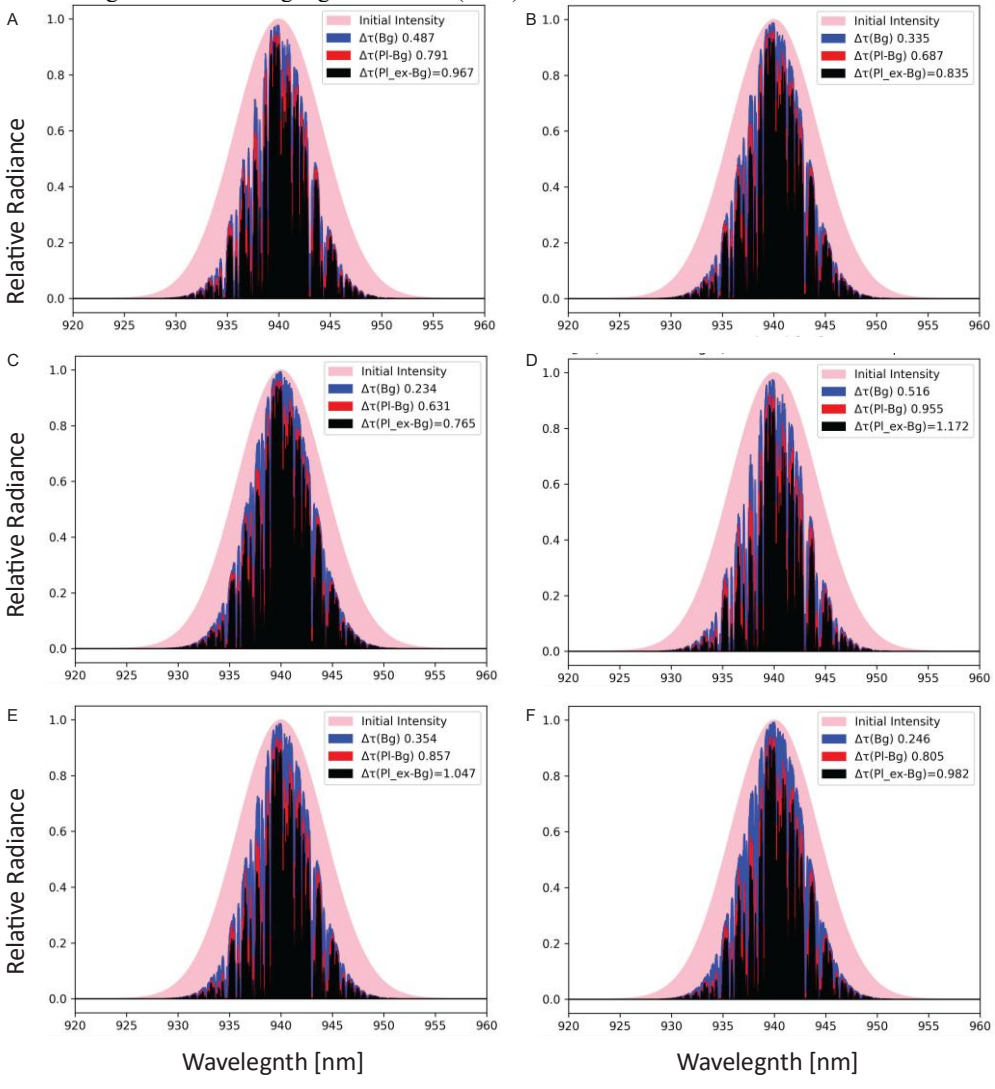

https://doi.org/10.5194/egusphere-2025-6430
Preprint. Discussion started: 29 January 2026

Figure A2 continue

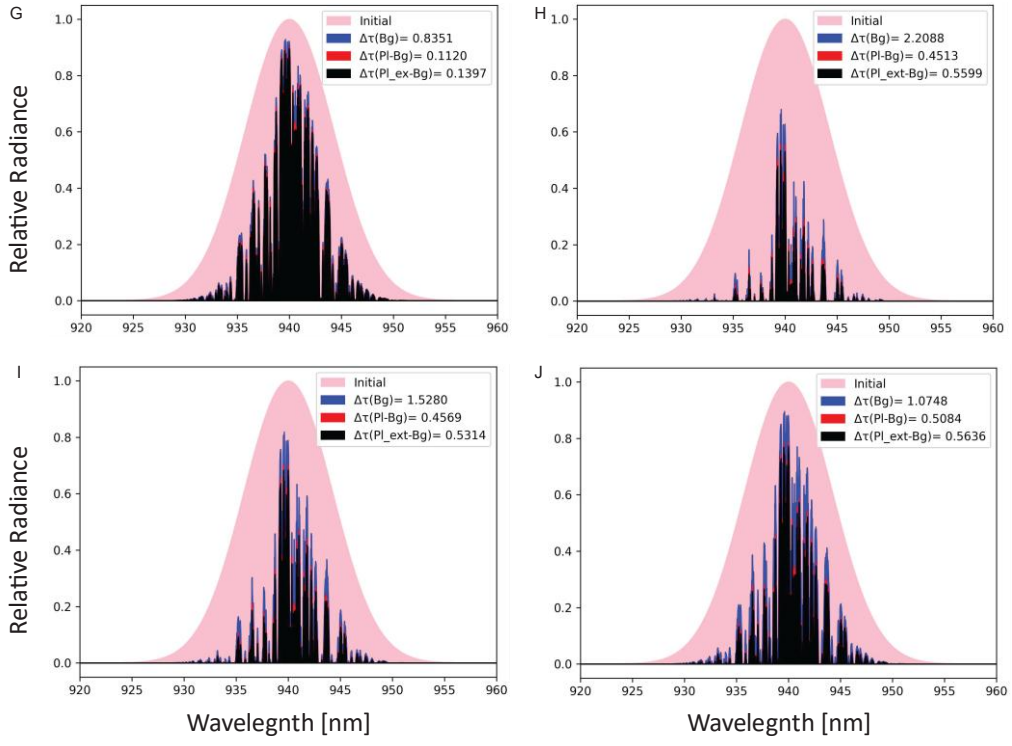

Code availability. *Refer to the corresponding author for inquiries.*

Video Supplements

https://doi.org/10.5446/s_1994

Author contribution: *Felipe Rojas Vilches Writing original draft, Writing, review & editing, data collection, data processing, Methodology, Modeling; Tobias P. Fischer Writing, supervised the project, review & editing, data collection, Methodology; Scott Nowicki1 Writing, supervised the project, review & editing, data collection; Methodology; Melissa Anne Pfeffer Writing, review & editing, Formal analysis; Felipe Aguilera Writing, review & editing, Formal analysis; Tom D. Pering Writing, review & editing, Methodology, Formal analysis; Thomas Wilkes Writing, review & editing; Susana Layana review & editing; Cristóbal González review & editing; Matthew Fricke review & editing; John Ericksen review & editing; Melanie Moses review & editing.*

Competing interests: *The authors declare that they have no conflict of interest.*

https://doi.org/10.5194/egusphere-2025-6430
Preprint. Discussion started: 29 January 2026

Acknowledgements: *The authors would like to thank the US National Science Foundation, National Robotics Initiative for grant NRI-2024520 to Melanie Moses and Tobias Fischer. We also would like to express our sincere gratitude to the Community of Talabre for granting access to Lascar Volcano and for allowing us to stay and work with them. We thank students Lexi Kenis (UNM), Mauricio Aguilera, Alexander Scheinost, and Michelle Villalta (Universidad Católica del Norte) for assistance during field work at Lascar Volcano. We would like to thank Dr. Thorvaldur Thordarson (University of Iceland) and Dr. Bruce Hougton (University of Hawaii), their students Jóna Sigurlína Pálmadóttir and Caroline Tisdale, along with Arianna Soldati (North Carolina State University), Laura Wainman (University of Leeds), Josefa Sepúlveda-Araya (University of Leeds), and Nicolas Fischer for their help and assistance during the 2023 Litli Hrútur eruption field work.*

6 References

Aguilera, F., Apaza, F., Del Carpio, J., Grosse, P., Jiménez, N., Ureta, G., Inostroza, M., Báez, W., Layana, S., Gonzalez, C., Rivera, M., Ortega, M., Gonzalez, R., Iriarte, R. Advances in scientific understanding of the Central Volcanic Zone of the Andes: a review of contributing factors. Bull Volcanol 84, 22. https://doi.org/10.1007/s00445-022-01526-y, 2022.

Aiuppa, A., Federico, C., Giudice, G., and Gurrieri, S. Chemical mapping of a fumarolic field: La Fossa Crater, Vulcano Island (Aeolian Islands, Italy): Geophysical Research Letters, v. 32, p. 1–4, doi:10.1029/2005GL023207, 2005.

Aiuppa, A., Fischer, T.P., Plank, T., Bani, P. CO2 flux emissions from the Earth's most actively degassing volcanoes, 2005–2015. Sci Rep 9, 5442. https://doi.org/10.1038/s41598-019-41901-y, 2019.

Arellano, S., Hall, M., Ayala, E. Spectroscopic remote sensing of volcanic gases: The Ecuadorian case. Optica Pura y aplicada, III Workshop LIDAR mesur. in Latinamerica 39, 99–108, 2006.

Arellano, S.R. Studies of volcanic plumes with spectroscopic remote sensing techniques --- DOAS and FTIR observations at Karymsky, Nyiragongo, Popocatépetl and Tungurahua: , p. 93, 2013.

Battaglia, A., De Moor, J.M., Aiuppa, A., Avard, G., Bakkar, H., Bitetto, M., Mora Fernández, M.M., Kelly, P., Giudice, G., Delle Donne, D., Villalobos, H. Insights Into the Mechanisms of Phreatic Eruptions From Continuous High Frequency Volcanic Gas Monitoring: Rincón de la Vieja Volcano, Costa Rica. Front. Earth Sci. 6, 247. https://doi.org/10.3389/feart.2018.00247, 2019.

Bluth, G.J.S., Shannon, J.M., Watson, I.M., Prata, A.J., and Realmuto, V.J. Development of an ultra-violet digital camera for volcanic SO2 imaging: Journal of Volcanology and Geothermal Research, v. 161, p. 47–56, https://doi.org/10.1016/j.jvolgeores.2006.11.004, 2007.

Bucarey, C., Arellano, S., Velasquez, G., Galle, B., SO2 flux of -LASCAR- volcano from the NOVAC data-base, [Data set] , v.001, https://doi.org/10.17196/novac.lascar.001, 2020.

https://doi.org/10.5194/egusphere-2025-6430
Preprint. Discussion started: 29 January 2026

Burton, M.R., Oppenheimer, C., Horrocks, L.A., Francis, P.W. Remote sensing of CO2 and H2O emission rates from Masaya volcano, Nicaragua. Geology 28, 915–918. https://doi.org/10.1130/0091-7613(2000)28%253C915:RSOCAH%253E2.0.CO;2, 2000.

Castillo, J.E., Weibel, J.A., Garimella, S.V. The effect of relative humidity on dropwise condensation dynamics. International Journal of Heat and Mass Transfer 80, 759–766. https://doi.org/10.1016/j.ijheatmasstransfer.2014.09.080, 2015.

Cerminara, M., Esposti Ongaro, T., Valade, S., Harris, A.J.L. Volcanic plume vent conditions retrieved from infrared images: A forward and inverse modeling approach. Journal of Volcanology and Geothermal Research 300, 129–147. https://doi.org/10.1016/j.jvolgeores.2014.12.015, 2015.

Cheremkhin, P.A., Lesnichii, V.V., Petrov, N.V. Use of spectral characteristics of DSLR cameras with Bayer filter sensors. J. Phys.: Conf. Ser. 536, 012021. https://doi.org/10.1088/1742-6596/536/1/012021, 2014.

Conde, V., Robidoux, P., Avard, G., Galle, B., Aiuppa, A., Muñoz, A., and Giudice, G. Measurements of volcanic SO2 and CO2 fluxes by combined DOAS, Multi-GAS and FTIR observations: a case study from Turrialba and Telica volcanoes: International Journal of Earth Sciences, v. 103, p. 2335–2347, https://doi.org/10.1007/s00531-014-1040-7, 2014.

de Moor, J.M., Fischer, T.P., Sharp, Z.D., King, P.L., Wilke, M., Botcharnikov, R.E., Cottrell, E., Zelenski, M., Marty, B., Klimm, K., Rivard, C., Ayalew, D., Ramirez, C., Kelley, K.A. Sulfur degassing at Erta Ale (Ethiopia) and Masaya (Nicaragua) volcanoes: Implications for degassing processes and oxygen fugacities of basaltic systems. Geochem Geophys Geosyst 14, 4076–4108. https://doi.org/10.1002/ggge.20255, 2013.

De Moor, J.M., Barry, P.H., Rodríguez, A., Aguilera, F., Aguilera, M., Gonzalez, C., Layana, S., Chiodi, A., Apaza, F., Masias, P., Kern, C., Barnes, J.D., Cullen, J.T., Bastoni, D., Bastianoni, A., Cascone, M., Jimenez, C., Salas-Navarro, J., Ramírez, C., Jessen, G.L., Giovannelli, D., Lloyd, K.G. Origins and fluxes of gas emissions from the Central Volcanic Zone of the Andes. Journal of Volcanology and Geothermal Research 466, 108382. https://doi.org/10.1016/j.jvolgeores.2025.108382, 2025.

Esse, B., Burton, M., Hayer, C., Pfeffer, M.A., Barsotti, S., Theys, N., Barnie, T., and Titos, M., Satellite derived SO2 emissions from the relatively low-intensity, effusive 2021 eruption of Fagradalsfjall, Iceland: Earth and Planetary Science Letters, v. 619, p. 118325, https://doi.org/10.1016/j.epsl.2023.118325, 2023.

Fischer, T.P., Giggenbach, W.F., Sano, Y., Williams, S.N.. Fluxes and sources of volatiles discharged from Kudryavy, a subduction zone volcano, Kurile Islands. Earth and Planetary Science Letters 160, 81–96. https://doi.org/10.1016/S0012-821X(98)00086-7, 1998.

Fischer, T.P., Fluxes of volatiles (H2O, CO2, N2, Cl, F) from arc volcanoes: GEOCHEMICAL JOURNAL, v. 42, p. 21–38, https://doi.org/10.2343/geochemj.42.21, 2008.

Fischer, T.P., and Chiodini, G., Volcanic, Magmatic and Hydrothermal Gases, in Sigurdsson & Houghton & McNutt & Rymer & Stix ed., The Encyclopedia of Volcanoes, Elsevier, p. 779–797.

Fischer, T. P. et al., 2019, The emissions of CO2 and other volatiles from the world's subaerial volcanoes: Scientific Reports, v. 9, p. 1–11, https://doi.org/10.1038/s41598-019-54682-1, 2015.

https://doi.org/10.5194/egusphere-2025-6430
Preprint. Discussion started: 29 January 2026

Fischer, T.P., Mandon, C.L., Nowicki, S., Ericksen, J., Vilches, F.R., Pfeffer, M.A., Aiuppa, A., Bitetto, M., Vitale, A., Fricke, G.M., Moses, M.E., Stefánsson, A. CO2 emissions during the 2023 Litli Hrútur eruption in Reykjanes, Iceland: δ13C tracks magma degassing. Bulletin of Volcanology 86. https://doi.org/10.1007/s00445-024-01751-7, 2024.

Gaete, A., Walter, T.R., Bredemeyer, S., Zimmer, M., Kujawa, C., Franco Marin, L., San Martin, J., and Bucarey Parra, C., Processes culminating in the 2015 phreatic explosion at Lascar volcano, Chile, evidenced by multiparametric data: Natural Hazards and Earth System Sciences, v. 20, p. 377–397, https://doi.org/10.5194/nhess-20-377-2020, 2020.

Galle, B., Oppenheimer, C., Geyer, A., McGonigle, A.J.S., Edmonds, M., and Horrocks, L., A miniaturised ultraviolet spectrometer for remote sensing of SO2 fluxes: A new tool for volcano surveillance: Journal of Volcanology and Geothermal Research, v. 119, p. 241–254, https://doi.org/10.1016/S0377-0273(02)00356-6, 2003.

Gardeweg, M.C., Sparks, R.S.J., and Matthews, S., Evolution of Lascar volcano, northern Chile: Journal of the Geological Society, v. 155, p. 89–104, https://doi.org/10.1144/gsjgs.155.1.0089, 1998.

Giggenbach, W.F., Variations in the chemical and isotopic composition of fluids discharged from the Taupo Volcanic Zone, New Zealand: Journal of Volcanology and Geothermal Research, v. 68, p. 89–116, https://doi.org/10.1016/0377-0273(95)00009-J, 1996.

Girona, T., Costa, F., Taisne, B., Aggangan, B., and Ildefonso, S., Fractal degassing from Erebus and Mayon volcanoes revealed by a new method to monitor H2O emission cycles: Journal of Geophysical Research: Solid Earth, v. 120, p. 2988–3002, https://doi.org/10.1002/2014JB011797, 2015.

Global Volcanism Program. Volcanoes of the World - Lascar (355100) in [Database] Volcanoes of the World (v. 5.1.3; 13 Oct 2023). Distributed by Smithsonian Institution, compiled by Venzke, E, https://volcano.si.edu/volcano.cfm?vn=355100, 2023.

Global Volcanism Program. “Report on Lascar (Chile) (Bennis, K.L., and Venzke, E., Eds.).” 48:3. Bulletin of the Global Volcanism Network. Smithsonian Institution. https://volcano.si.edu/showreport.cfm?doi=10.5479/si.GVP.BGVN202303-355100. 2022.

Halldórsson, S.A., Marshall, E.W., Caracciolo, A., Matthews, S., Bali, E., Rasmussen, M.B., Ranta, E., Robin, J.G., Guðfinnsson, G.H., Sigmarsson, O., Maclennan, J., Jackson, M.G., Whitehouse, M.J., Jeon, H., Van Der Meer, Q.H.A., Mibei, G.K., Kalliokoski, M.H., Repczynska, M.M., Rúnarsdóttir, R.H., Sigurðsson, G., Pfeffer, M.A., Scott, S.W., Kjartansdóttir, R., Kleine, B.I., Oppenheimer, C., Aiuppa, A., Ilyinskaya, E., Bitetto, M., Giudice, G., Stefánsson, A. Rapid shifting of a deep magmatic source at Fagradalsfjall volcano, Iceland. Nature 609, 529–534. https://doi.org/10.1038/s41586-022-04981-x

Halthore, R.N., Eck, T.F., Holben, B.N., and Markham, B.L., 1997, Sun photometric measurements of atmospheric water vapor column abundance in the 940-nm band: Journal of Geophysical Research: Atmospheres, v. 102, p. 4343–4352, https://doi.org/10.1029/96JD03247, 2022.

Harris, A., Ripepe, M. Temperature and dynamics of degassing at Stromboli. Journal of Geophysical Research: Solid Earth 112, 18. https://doi.org/10.1029/2006JB004393, 2007.

Herzog, M., Graf, H.-F., Textor, C., Oberhuber, J.M. The effect of phase changes of water on the development of volcanic plumes. Journal of Volcanology and Geothermal Research 87, 55–74. https://doi.org/10.1016/S0377-0273(98)00100-0, 1998.

https://doi.org/10.5194/egusphere-2025-6430
Preprint. Discussion started: 29 January 2026

Horrocks, L.A., Oppenheimer, C., Burton, M.R., Duffell, H.J., Davies, N.M., Martin, N.A., Bell, W. Open-path Fourier transform infrared spectroscopy of SO_2: An empirical error budget analysis, with implications for volcano monitoring. J. Geophys. Res. 106, 27647–27659. https://doi.org/10.1029/2001JD000343, 2001.

Ingold, T., Schmid, B., Mätzler, C., Demoulin, P., and Kämpfer, N., Modeled and empirical approaches for retrieving columnar water vapor from solar transmittance measurements in the 0.72, 0.82, and 0.94 µm absorption bands: Journal of Geophysical Research Atmospheres, v. 105, p. 24327–24343, https://doi.org/10.1029/2000JD900392, 2000.

Jongebloed, U.A., Schauer, A.J., Cole-Dai, J., Larrick, C.G., Wood, R., Fischer, T.P., Carn, S.A., Salimi, S., Edouard, R.S., Shai, S., Geng, L. and Alexander, B. Underestimated Passive Volcanic Sulfur Degassing Implies Overestimated Anthropogenic Aerosol Forcing. Geophys Res. Lett., https://doi.org/10.1029/2022GL102061, 2023.

Kantzas, E.P., McGonigle, A.J.S., Tamburello, G., Aiuppa, A., and Bryant, R.G., Protocols for UV camera volcanic SO2 measurements: Journal of Volcanology and Geothermal Research, v. 194, p. 55–60, https://doi.org/10.1016/j.jvolgeores.2010.05.003, 2010.

Kazahaya, R., Varnam, M., Esse, B., Burton, M., Shinohara, H., and Ibarra, M., Behaviors of Redox-Sensitive Components in the Volcanic Plume at Masaya Volcano , Nicaragua : H 2 Oxidation and CO Preservation in Air: v. 10, p. 1–10, https://doi.org/10.3389/feart.2022.867562, 2022.

Kelley, K.A., Fischer, T.P.. Melt inclusion and gas perspectives on volatiles in subduction zones, in: Treatise on Geochemistry. Elsevier, pp. 745–771. https://doi.org/10.1016/B978-0-323-99762-1.00081-4, 2025.

Kern, C. Ultraviolet and visible remote sensing of volcanic gas emissions. Journal of Volcanology and Geothermal Research 468, 108423. https://doi.org/10.1016/j.jvolgeores.2025.108423, 2025.

Kelsey, V., Riley, S., Minschwaner, K. Atmospheric precipitable water vapor and its correlation with clear-sky infrared temperature observations. Atmos. Meas. Tech. 15, 1563–1576. https://doi.org/10.5194/amt-15-1563-2022, 2022.

Kern, C., Kick, F., Lübcke, P., Vogel, L., Wöhrbach, M., and Platt, U., Theoretical description of functionality, applications, and limitations of SO2 cameras for the remote sensing of volcanic plumes: Atmospheric Measurement Techniques, v. 3, p. 733–749, https://doi.org/10.5194/amt-3-733-2010, 2010.

Kern, C., The difficulty of measuring the absorption of scattered sunlight by H2O and CO2 in volcanic plumes: A comment on pering et al. “A novel and inexpensive method for measuring volcanic plume water fluxes at high temporal resolution,” Remote Sens. 2017, 9, 14: Remote Sensing, v. 9, https://doi.org/10.3390/rs9060534, 2017.

Kern, C., Masias, P., Apaza, F., Reath, K.A., and Platt, U., Remote measurement of high preeruptive water vapor emissions at Sabancaya volcano by passive differential optical absorption spectroscopy: Journal of Geophysical Research: Solid Earth, v. 122, p. 3540–3564, https://doi.org/10.1002/2017JB014020, 2017.

Krmíček, L., Troll, V. R., Thordarson, T., Brabec, M., Moreland, W. M., & Maťo, A. The 2023 Litli-Hrútur eruption of the Fagradalsfjall fires, SW-Iceland: Insights from trace element compositions of olivine. Czech Polar Reports, 13, 257–270. https://doi.org/10.5817/CPR2023-2-20, 2023.

https://doi.org/10.5194/egusphere-2025-6430
Preprint. Discussion started: 29 January 2026

Kuhn, L., Kuhn, J., Wagner, T., Platt, U. The NO2 camera based on gas correlation spectroscopy. Atmos. Meas. Tech. 15, 1395–1414. https://doi.org/10.5194/amt-15-1395-2022, 2022.

Langer, G., Hochreiner, A., Burgholzer, P., and Berer, T., A webcam in Bayer-mode as a light beam profiler for the near infra-red: Optics and Lasers in Engineering, v. 51, p. 571–575, doi:10.1016/j.optlaseng.2012.12.010, 2013.

Layana, S., Aguilera, F., Rojo, G., Vergara, Á., Salazar, P., Quispe, J., Urra, P., and Urrutia, D., Volcanic Anomalies Monitoring System (VOLCANOMS), a low-cost volcanic monitoring system based on Landsat images: Remote Sensing, v. 12, https://doi.org/10.3390/rs12101589, 2020.

Lopez, T., Thomas, H.E., Prata, A.J., Amigo, A., Fee, D., and Moriano, D., Volcanic plume characteristics determined using an infrared imaging camera: Journal of Volcanology and Geothermal Research, v. 300, p. 148–166, https://doi.org/10.1016/j.jvolgeores.2014.12.009, 2014.

Lübcke, P., Bobrowski, N., Illing, S., Kern, C., Alvarez Nieves, J.M., Vogel, L., Zielcke, J., Delgado Granados, H., Platt, U. On the absolute calibration of SO2 cameras. Atmos. Meas. Tech. 6, 677–696. https://doi.org/10.5194/amt-6-677-2013, 2013.

Matthews, S., Jones, A.P., and Gardeweg, M.C., Lascar volcano, northern Chile; evidence for steady-state disequilibrium: Journal of Petrology, v. 35, p. 401–432, https://doi.org/10.1093/petrology/35.2.401, 1994.

Mather, T.A., Pyle, D.M., Oppenheimer, C. Tropospheric volcanic aerosol, in: Robock, A., Oppenheimer, Clive (Eds.), Geophysical Monograph Series. American Geophysical Union, Washington, D. C., pp. 189–212. https://doi.org/10.1029/139GM12, 2003.

Matsushima, N., and H. Shinohara. “Visible and Invisible Volcanic Plumes.” Geophysical Research Letters 33 (24). https://doi.org/10.1029/2006GL026506, 2006.

McGonigle, A. J. S., D. R. Hilton, T. P. Fischer, and C. Oppenheimer. “Plume Velocity Determination for Volcanic SO2 Flux Measurements.” Geophysical Research Letters 32 (11). https://doi.org/10.1029/2005GL022470, 2005.

McGonigle, A. J. S., A. Aiuppa, M. Ripepe, E. P. Kantzas, and G. Tamburello. “Spectroscopic Capture of 1 Hz Volcanic SO2 Fluxes and Integration with Volcano Geophysical Data.” Geophysical Research Letters 36 (21). https://doi.org/10.1029/2009GL040494, 2009.

McRae, G.J. A Simple Procedure for Calculating Atmospheric Water Vapor Concentration. Journal of the Air Pollution Control Association 30, 394–394. https://doi.org/10.1080/00022470.1980.10464362, 1980.

Menard, G., Moune, S., Vlastélic, I., Aguilera, F., Valade, S., Bontemps, M., and González, R., Gas and aerosol emissions from Lascar volcano (Northern Chile): Insights into the origin of gases and their links with the volcanic activity: Journal of Volcanology and Geothermal Research, v. 287, p. 51–67, https://doi.org/10.1016/j.jvolgeores.2014.09.004, 2014.

Momoi, M., Irie, H., Sekiguchi, M., Nakajima, T., Takenaka, H., Miura, K., and Aoki, K., Rapid, accurate computation of narrow-band sky radiance in the 940 nm gas absorption region using the correlated k-distribution method for sun-photometer observations: Progress in Earth and Planetary Science, v. 9, https://doi.org/10.1186/s40645-022-00467-6, 2022.

Mori, T., and Burton, M., The SO2 camera: A simple, fast and cheap method for ground-based imaging of SO2 in volcanic plumes: Geophysical Research Letters, v. 33, p. 1–5, https://doi.org/10.1029/2006GL027916, 2006.

https://doi.org/10.5194/egusphere-2025-6430
Preprint. Discussion started: 29 January 2026

Moussallam, Y., Rose-Koga, E.F., Fischer, T.P., Georgeais, G., Lee, H.J., Birnbaum, J., Pfeffer, M.A., Barnie, T., Regis, E.. Kinetic Isotopic Degassing of CO2 During the 2021 Fagradalsfjall Eruption and the δ13 C Signature of the Icelandic Mantle. Geochem Geophys Geosyst 25, e2024GC011997. https://doi.org/10.1029/2024GC011997, 2024.

Moussallam, Y., Tamburello, G., Peters, N., Apaza, F., Schipper, C.I., Curtis, A., Aiuppa, A., Masias, P., Boichu, M., Bauduin, S., Barnie, T., Bani, P., Giudice, G., Moussallam, M. Volcanic gas emissions and degassing dynamics at Ubinas and Sabancaya volcanoes; implications for the volatile budget of the central volcanic zone. GVGR 343, 181–191. https://doi.org/10.1016/j.jvolgeores.2017.06.027, 2017.

Nowicki, S. Sulfur Hexafluoride Imaging System. U.S. Patent US 2020/0132646 A1, 8 pp., issued 30 Apr. 2020, U.S. Patent and Trademark Office, 2020.

Oppenheimer, C., Francis, P., Burton, M., Maciejewski, A.J.H., Boardman, L. Remote measurement of volcanic gases by Fourier transform infrared spectroscopy. Applied Physics B: Lasers and Optics 67, 505–515. https://doi.org/10.1007/s003400050536, 1998.

Oppenheimer, C., Bani, P., Calkins, J.A., Burton, M.R., Sawyer, G.M. Rapid FTIR sensing of volcanic gases released by Strombolian explosions at Yasur volcano, Vanuatu. Appl. Phys. B 85, 453–460. https://doi.org/10.1007/s00340-006-2353-4, 2006.

Oppenheimer, C., Fischer, T.P., and Scaillet, B., Volcanic Degassing: Process and Impact: Elsevier Ltd., v. 4, 111–179 p., https://doi.org/10.1016/B978-0-08-095975-7.00304-1, 2013.

Pedersen, G. B. M., Belart, J. M. C., Óskarsson, B. V., Gunnarson, S. R., Gudmundsson, M. T., Reynolds, H. I., Valsson, G., Högnadóttir, T., Pinel, V., Parks, M. M., Drouin, V., Askew, R. A., Dürig, T., and Þrastarson, R. H.: Volume, effusion rates and lava hazards of the 2021, 2022 and 2023 Reykjanes fires: Lessons learned from near real-time photogrammetric monitoring, EGU General Assembly 2025, Vienna, Austria, EGU24-10724, https://doi.org/10.5194/egusphere-egu24-10724, 2024.

Pérez-Ramírez, D., Navas-Guzmán, F., Lyamani, H., Fernández-Gálvez, J., Olmo, F.J., and Alados-Arboledas, L., Retrievals of precipitable water vapor using star photometry: Assessment with Raman lidar and link to sun photometry: Journal of Geophysical Research Atmospheres, v. 117, p. 1–10, https://doi.org/10.1029/2011JD016450, 2012.

Pering, T.D., Tamburello, G., McGonigle, A.J.S., Hanna, E., Aiuppa, A. Correlation of oscillatory behaviour in Matlab using wavelets. Computers & Geosciences 70, 206–212. https://doi.org/10.1016/j.cageo.2014.06.006, 2014.

Pering, T.D., McGonigle, A.J.S., Tamburello, G., Aiuppa, A., Bitetto, M., Rubino, C., and Wilkes, T.C., A novel and inexpensive method for measuring volcanic plume water fluxes at high temporal resolution: Remote Sensing, v. 9, p. 1–13, https://doi.org/10.3390/rs9020146, 2017.

Pfeffer, M.A., Arellano, S., Barsotti, S., Petersen, G.N., Barnie, T., Ilyinskaya, E., Hjörvar, T., Bali, E., Pedersen, G.B.M., Guðmundsson, G.B., Vogfjörð, K., Ranta, E.J., Óladóttir, B.A., Edwards, B.A., Moussallam, Y., Stefánsson, A., Scott, S.W., Smekens, J.-F., Varnam, M., Titos, M. SO2 emission rates and incorporation into the air pollution dispersion forecast during

https://doi.org/10.5194/egusphere-2025-6430
Preprint. Discussion started: 29 January 2026

the 2021 eruption of Fagradalsfjall, Iceland. Journal of Volcanology and Geothermal Research 449, 108064. https://doi.org/10.1016/j.jvolgeores.2024.108064, 2024.

Platt, U., Bobrowski, N., and Butz, A., Ground-based remote sensing and imaging of volcanic gases and quantitative determination of multi-species emission fluxes: Geosciences (Switzerland), v. 8, doi:10.3390/geosciences8020044, 2018.

Plank, T., Kelley, K.A., Zimmer, M.M., Hauri, E.H., Wallace, P.J. Why do mafic arc magmas contain ~4wt% water on average? Earth and Planetary Science Letters 364, 168–179. https://doi.org/10.1016/j.epsl.2012.11.044, 2013.

Prata, A.J. Satellite detection of hazardous volcanic clouds and the risk to global air traffic. Nat Hazards 51, 303–324. https://doi.org/10.1007/s11069-008-9273-z, 2009.

Radu, I.-B., Skogby, H., Troll, V.R., Deegan, F.M., Geiger, H., Müller, D., Thordarson, T. Water in clinopyroxene from the 2021 Geldingadalir eruption of the Fagradalsfjall Fires, SW-Iceland. Bull Volcanol 85, 31. https://doi.org/10.1007/s00445-023-01641-4, 2023.

Robock, A. Volcanic eruptions and climate. Reviews of Geophysics 38, 191–219. https://doi.org/10.1029/1998RG000054, 2000.

Rothman, L.S., Gordon, I.E., Babikov, Y., Barbe, A., Chris Benner, D., Bernath, P.F., Birk, M., Bizzocchi, L., Boudon, V., Brown, L.R., Campargue, A., Chance, K., Cohen, E.A., Coudert, L.H., Devi, V.M., Drouin, B.J., Fayt, A., Flaud, J.-M., Gamache, R.R., Harrison, J.J., Hartmann, J.-M., Hill, C., Hodges, J.T., Jacquemart, D., Jolly, A., Lamouroux, J., Le Roy, R.J., Li, G., Long, D.A., Lyulin, O.M., Mackie, C.J., Massie, S.T., Mikhailenko, S., Müller, H.S.P., Naumenko, O.V., Nikitin, A.V., Orphal, J., Perevalov, V., Perrin, A., Polovtseva, E.R., Richard, C., Smith, M.A.H., Starikova, E., Sung, K., Tashkun, S., Tennyson, J., Toon, G.C., Tyuterev, Vl.G., Wagner, G. The HITRAN2012 molecular spectroscopic database. Journal of Quantitative Spectroscopy and Radiative Transfer 130, 4–50. https://doi.org/10.1016/j.jqsrt.2013.07.002, 2013.

Sæmundsson, K., Sigurgeirsson, M.Á., Friðleifsson, G.Ó. Geology and structure of the Reykjanes volcanic system, Iceland. Journal of Volcanology and Geothermal Research 391, 106501. https://doi.org/10.1016/j.jvolgeores.2018.11.022, 2020.

Shinohara, H., A new technique to estimate volcanic gas composition: plume measurements with a portable multi-sensor system: Journal of Volcanology and Geothermal Research, v. 143, p. 319–333, https://doi.org/10.1016/j.jvolgeores.2004.12.004, 2005.

Sigurdsson, H., and Carey, S., Volcanic disasters in Latin America and the 13th November 1985 eruption of Nevado del Ruiz volcano in Colombia: Disasters, v. 10, p. 205–216, https://doi.org/10.1111/j.1467-7717.1986.tb00590.x, 1986.

Schmidt, A., Carslaw, K.S., Mann, G.W., Rap, A., Pringle, K.J., Spracklen, D.V., Wilson, M., Forster, P.M. Importance of tropospheric volcanic aerosol for indirect radiative forcing of climate. Atmos. Chem. Phys. 12, 7321–7339. https://doi.org/10.5194/acp-12-7321-2012, 2012.

Stechern, A., Blum-Oeste, M., Botcharnikov, R.E., Holtz, F., Wörner, G. Magma storage conditions of Lascar andesites, central volcanic zone, Chile. Eur. J. Mineral. 36, 721–748. https://doi.org/10.5194/ejm-36-721-2024, 2024.

https://doi.org/10.5194/egusphere-2025-6430
Preprint. Discussion started: 29 January 2026

Stix, J., De Moor, J.M., Rüdiger, J., Alan, A., Corrales, E., D'Arcy, F., Diaz, J.A., Liotta, M. Using Drones and Miniaturized Instrumentation to Study Degassing at Turrialba and Masaya Volcanoes, Central America. JGR Solid Earth 123, 6501–6520. https://doi.org/10.1029/2018JB015655, 2018.

Tamburello, G., Hansteen, T.H., Bredemeyer, S., Aiuppa, A., Tassi, F. Gas emissions from five volcanoes in northern Chile and implications for the volatiles budget of the Central Volcanic Zone. Geophysical Research Letters 41, 4961–4969. https://doi.org/10.1002/2014GL060653, 2014.

Tamburello, G., Ratiocalc: Software for processing data from multicomponent volcanic gas analyzers: Computers and Geosciences, v. 82, p. 63–67, https://doi.org/10.1016/j.cageo.2015.05.004, 2015.

Tassi, F., Aguilera, F., Vaselli, O., Medina, E., Tedesco, D., Delgado Huertas, A., Poreda, R., and Kojima, S., The magmatic- and hydrothermal-dominated fumarolic system at the Active Crater of Lascar volcano, northern Chile: Bulletin of Volcanology, v. 71, p. 171–183, https://doi.org/10.1007/s00445-008-0216-z, 2009.

Thordarson, T., and G. Larsen. "Volcanism in Iceland in Historical Time: Volcano Types, Eruption Styles and Eruptive History." *Journal of Geodynamics* 43 (1): 118–52. https://doi.org/10.1016/j.jog.2006.09.005, 2007.

Thordarson, T., Hoskuldsson, A., Jónsdottir, I., Moreland, W., Houghton, B.F., Pálmadóttir, J.S., Valdimarsdóttir, I.K., Payet--Clerc, M., Alvarez, D.B.D.S.G., Grech-Licari, J., Gallagher, C.R., Stroganova, L., Askew, R.A., Torfadóttir, H.K., Eibl, E.P.S., Pétursdóttir, L.B., Troll, V.R. The 2021, 2022 and 2023 eruptions of Fagradalsfjall Fires, Reykjanes Peninsula Iceland. Presented at the AGU23, AGU. https://ui.adsabs.harvard.edu/abs/2023AGUFM.V32A..02T, 2023.

Wagner, W., and Pruß, A., The IAPWS Formulation 1995 for the Thermodynamic Properties of Ordinary Water Substance for General and Scientific Use: Journal of Physical and Chemical Reference Data, v. 31, p. 387–535, https://doi.org/10.1063/1.1461829, 2002.

Wallace, P.J. Volatiles in subduction zone magmas: concentrations and fluxes based on melt inclusion and volcanic gas data. Journal of Volcanology and Geothermal Research 140, 217–240. https://doi.org/10.1016/j.jvolgeores.2004.07.023, 2005.

Werner, C., Fischer, T.P., Aiuppa, A., Edmonds, M., Cardellini, C., Carn, S., Chiodini, G., Cottrell, E., Burton, M., Shinohara, H., Allard, P. Carbon Dioxide Emissions from Subaerial Volcanic Regions: Two Decades in Review, in: Orcutt, B.N., Daniel, I., Dasgupta, R. (Eds.), Deep Carbon. Cambridge University Press, pp. 188–236. https://doi.org/10.1017/9781108677950.008, 2019.

Wilkes, T.C., McGonigle, A.J.S., Pering, T.D., Taggart, A.J., White, B.S., Bryant, R.G., and Willmott, J.R., Ultraviolet imaging with low cost smartphone sensors: Development and application of a raspberry pi-based UV camera: Sensors (Switzerland), v. 16, https://doi.org/10.3390/s16101649, 2016.

Wilkes, T.C., Pering, T.D., McGonigle, A.J.S., Tamburello, G., and Willmott, J.R., A low-cost smartphone sensor-based UV camera for volcanic SO2 emission measurements: Remote Sensing, v. 9, p. 1–11, https://doi.org/10.3390/rs9010027, 2017.

Wilkes, T.C., Stanger, L.R., Willmott, J.R., Pering, T.D., McGonigle, A.J.S., and England, R.A., The development of a low-cost, near infrared, high-temperature thermal imaging system and its application to the retrieval of accurate lava lake temperatures at Masaya volcano, Nicaragua: Remote Sensing, v. 10, https://doi.org/10.3390/rs10030450, 2018.

https://doi.org/10.5194/egusphere-2025-6430
Preprint. Discussion started: 29 January 2026

Wilkes, T.C., Pering, T.D., Aguilera, F., Layana, S., Nadeau, P., Kern, C., McGonigle, A.J.S., Aguilera, M., Zhu, C. A new permanent, low-cost, low-power SO2 camera for continuous measurement of volcanic emissions. Front. Earth Sci. 11, 1088992. https://doi.org/10.3389/feart.2023.1088992, 2023.

Williams, S.N., Schaefer, S.J., Marta Lucia Calvache, V., Lopez, D., Global carbon dioxide emission to the atmosphere by volcanoes. Geochimica et Cosmochimica Acta 56, 1765–1770. https://doi.org/10.1016/0016-7037(92)90243-C, 1992.

Xiong, Y., Wu, K., Yu, G., Chen, Z., Liu, L., Li, F. Real-Time Monitoring of SO2 Emissions Using a UV Camera with Built-in NO2 and Aerosol Corrections. Sensors 22, 3900. https://doi.org/10.3390/s22103900, 2022.